

MODAL IDENTIFICATION OF STRUCTURES USING EULERIAN-PHASE
BASED VIDEO MOTION MAGNIFICATION AND ANALYSIS

A THESIS SUBMITTED TO
THE GRADUATE SCHOOL OF NATURAL AND APPLIED SCIENCES
OF
MIDDLE EAST TECHNICAL UNIVERSITY

BY

KADYRBEK ISMAILOV

IN PARTIAL FULFILLMENT OF THE REQUIREMENTS
FOR
THE DEGREE OF MASTER OF SCIENCE
IN
CIVIL ENGINEERING

JANUARY 2020

Approval of the thesis:

**MODAL IDENTIFICATION OF STRUCTURES USING EULERIAN-PHASE
BASED VIDEO MOTION MAGNIFICATION AND ANALYSIS**

submitted by **KADYRBEK ISMAILOV** in partial fulfillment of the requirements for
the degree of **Master of Science in Civil Engineering Department, Middle East
Technical University** by,

Prof. Dr. Halil Kalıpçılar
Dean, Graduate School of **Natural and Applied Sciences**

Prof. Dr. Ahmet Türer
Head of Department, **Civil Engineering**

Prof. Dr. Ahmet Türer
Supervisor, **Civil Engineering, METU**

Examining Committee Members:

Prof. Dr. Alp Caner
Civil Engineering, METU

Prof. Dr. Ahmet Türer
Civil Engineering, METU

Prof. Dr. Erdem Canbay
Civil Engineering, METU

Assoc. Prof. Dr. Ozan Cem Çelik
Civil Engineering, METU

Assoc. Prof. Dr. Alper Aldemir
Civil Engineering, Hacettepe University

Date: 31.01.2020

I hereby declare that all information in this document has been obtained and presented in accordance with academic rules and ethical conduct. I also declare that, as required by these rules and conduct, I have fully cited and referenced all material and results that are not original to this work.

Name, Surname: Kadyrbek Ismailov

Signature:

ABSTRACT

MODAL IDENTIFICATION OF STRUCTURES USING EULERIAN-PHASE BASED VIDEO MOTION MAGNIFICATION AND ANALYSIS

Ismailov, Kadyrbek
Master of Science, Civil Engineering
Supervisor: Prof. Dr. Ahmet Türer

January 2020, 72 pages

Structural identification (St-Id) and dynamic analysis have been crucial in civil engineering structures, mainly buildings and bridges. In order to observe the vibrations of structures, networks of high-sensitivity sensors have been used. There are several limitations of such monitoring systems including cost, labor, number of sensors, and installation. A recent method called phase-based video magnification can be utilized in civil engineering to have a practical visual approach instead of array of sensors. This method will be useful especially for tall and long structures like skyscrapers and long span bridges where distance between sensors is a problem for data acquisition. Furthermore, video based modal testing is more convenient; number and spatial distribution of pixels is advantageous. Use of HD video as an input and magnification of tiny motions, which are not seen by naked eyes, are studied in this thesis. The phase-based video magnification algorithm is used and improved to obtain resonant mode shapes and frequencies of simple structures through video based spectral analysis. Simple ruler and cello wire vibrations and two pedestrian bridges were used as test structures to validate results directly obtained from video recordings.

Keywords: Modal identification, phase-based video magnification

ÖZ

EULERIAN-FAZ TABANLI VIDEO BÜYÜTME KULLANILARAK YAPILARIN MODAL TANIMLAMA VE ANALİZİ

Ismailov, Kadyrbek
Yüksek Lisans, İnşaat Mühendisliği
Tez Danışmanı: Prof. Dr. Ahmet Türer

Ocak 2020, 72 sayfa

İnşaat mühendisliğinde Yapısal belirleme (St-Id) ve dinamik analiz, özellikle köprü ve binalar açısından çok önemlidir. Yapıların titreşimlerini gözlemlemek için yüksek hassasiyetli sensör ağları kullanılmaktadır. Bunun gibi izleme sistemlerinin maliyet, işçilik, sensör sayısı ve kurulum gibi birçok dezavantajları vardır. Faz tabanlı video büyütme adı verilen yeni bir yöntem ile çok sayıda noktadan ve sensörlerin kullanılmasını engelleyerek inşaat mühendisliğinde kullanılabilir. Bu yöntem, özellikle sensörler arasındaki mesafenin veri toplama için bir sorun olduğu gökdelenler ve uzun açık köprüler gibi yapılar için yararlı olabilir. Ayrıca, video tabanlı mod testi piksellerin sayısı ve uzamsal dağılımından dolayı daha avantajlıdır. Bu tezde HD videoyu bir girdi olarak kullanarak çıplak gözle görülemeyen küçük hareketlerin büyütülmesi incelenmiştir. Faz tabanlı video büyütme algoritması, video tabanlı spektral analiz yoluyla rezonant mod şekilleri ve basit yapıların frekanslarını elde etmek için kullanılmıştır ve geliştirilmiştir. Cetvel ve çello teli gibi basit yapıların ve iki yaya köprüsünün rezonant mode şekilleri ve frekansları doğrudan video kaydından elde edilmiştir.

Anahtar Kelimeler: Modsal tanımlama, faz tabanlı video büyütmesi

To my jojoshkas

ACKNOWLEDGEMENTS

My deepest gratitude to Prof. Dr. Ahmet Türer not only for his guidance and support but also for his understanding and patience. He provided me almost with all equipment that was used in this thesis, and he did not withhold his help even after working hours.

I also thank all my friends that have supported me during my undergraduate and graduate years. I would like to thank Beksultan Kubanychbekov for cooking “yumpat” and Doolos Aybek uulu for eating it with me. I also thank Talgat Buzurkanov for loosing me in PES, and Bektur Adilbaev for showing me weird American reality shows. I would like to thank Nursultan Mamaev for being such a loyal friend and calling me often, and Altynbek Musaev for being a loyal friend and not calling me ever. I thank Shabdanbek Kasymov for getting through our undergraduate years in physics with me. I thank Oğuzhan Uluyurt for cheering me at work, and Muzaffer Doğanay for accompanying me during projects and courses in MS. I thank Zuhale Demirci for interesting discussions with me, Samet Aytekin, Mohammed Ali Rahimi, Mustafa Yaşa, Gençay Çelik, Alim Yolalmaz for their friendship.

I would like to thank my parents Aniver Usmanov, Shazatkhon Usmanova and my brother Sardarbek Ismailov for their endless support, advices and just for being there for me, throughout all my life.

Lastly, I thank my lovely wife Nurzhan Beksultanova and our sweet son Batukhan Kadyrbek for moral support and for making this journey positively challenging. My wife helped me proof read this thesis if there any grammatical mistakes, that is all her fault. I also thank my son for waking me up in the mornings so that I work on this thesis and change his dipper.

TABLE OF CONTENTS

ABSTRACT	v
ÖZ.....	vi
ACKNOWLEDGEMENTS	viii
TABLE OF CONTENTS	ix
LIST OF TABLES	xi
LIST OF FIGURES	xii
LIST OF ABBREVIATIONS	xv
CHAPTERS	
1. INTRODUCTION	1
1.1. Importance of structural health monitoring (SHM).....	1
1.2. Modal identification as SHM method	2
1.3. Motion microscopy.....	4
1.4. Aim of the study	5
2. THEORETICAL BACKGROUND.....	7
2.1. Lagrangian and Eulerian approaches	7
2.2. Eulerian linear magnification	8
2.3. Phase-based motion magnification.....	11
2.3.1. Definition of phase	11
2.3.2. Global magnification of motion.....	13
2.3.3. Complex steerable pyramid	14
2.3.3.1. Local motion magnification of 1D image	15
2.3.3.2. Motion magnification of 2D image.....	18

2.3.3.3. Types and bounds of complex steerable filters.....	21
2.3.4. Limitations of phase-based motion magnification	22
3. EXPERIMENTAL RESULTS	25
3.1. Method verification.....	25
3.1.1. METU A4 Bridge cable experiment	25
3.1.2. Ruler experiment	28
3.1.3. Cello experiment	32
4. MODAL IDENTIFICATION OF METU BRIDGE	39
4.1. Bridge Architecture.....	39
4.2. Measurements with accelerometer.....	42
4.3. Finite element model (FEM).....	45
4.4. Measurements with camera.....	53
4.4.1. Video motion detection	53
4.4.2. Video motion magnification.....	56
4.5. Discussion and comparison.....	58
5. CONCLUSION	61
5.1. Limitations of current study	63
5.2. Future work	65
REFERENCES	67
APPENDICES	69
A. Additional accelerometer measurements on METU A1 Bridge deck.....	69

LIST OF TABLES

TABLES

Table 1. Table of comparison of theoretical and experimental results	31
Table 2. Data extracted from the cello videos.....	33
Table 3. Vibration modes of the bridge deck from accelerometer measurements.....	44
Table 4. Analysis property data table.....	49
Table 5. Table of spring properties of support.....	49
Table 6. Mode frequencies of calibrated and uncalibrated models (Hz)	50
Table 7. Comparison table of calibrated FEM, accelerometer measurements and video measurements	59
Table 8. Summary table of resonant frequency modes of METU A1 Bridge deck from accelerometer measurements	72

LIST OF FIGURES

FIGURES

Figure 1. Contact method for vibration detection.....	3
Figure 2. Video camera-based vibration detection	3
Figure 3. Lagrangian and Eulerian approaches	7
Figure 4. Motion magnification by Lagrangian approach	8
Figure 5. Motion magnification with linear approximation	10
Figure 6. Magnified noise of Linear magnification and Phase-based magnification	11
Figure 7. Phase representation in complex domain	12
Figure 8. Swap of amplitudes and phases of two different pictures	13
Figure 9. Gaussian windowing of complex sinusoid.....	15
Figure 10. Decomposition of the signal into wavelets	16
Figure 11 Motion magnification of 1D signal	17
Figure 12. Complex steerable filters.....	19
Figure 13. Work flow of motion magnification.....	20
Figure 14. Types of complex steerable filters	22
Figure 15. (a) Original frame. Magnified 100 times mode shapes of the cable: (b) first, (c) second, (d) third, (e) fourth, (f) fifth.	26
Figure 16. Mode frequencies of cable	27
Figure 17. Fixing point of the ruler	28
Figure 18. Power spectral density of smartphone accelerometer measurement.....	29
Figure 19. Power spectral density of phase measurement from video	30
Figure 20. Power spectral density of phase measurement from 5 seconds video.....	31
Figure 21. Power spectral density of phase measurement from 1 st left string excited Video-1, without frame rate adjustment	33
Figure 22. Power spectral density of phase measurement from 1 st left string excited Video-1, with frame rate adjustment to 240 fps	34

Figure 23. Power spectral density of phase measurement from 2 nd left string excited Video-4, without frame rate adjustment.....	35
Figure 24. Power spectral density of phase measurement from 2 nd left string excited Video-4, with frame rate adjustment to 240 fps.....	35
Figure 25. 1 st left string motion magnification: (a) Original frame, (b) 20 times magnified frame, (c) magnified frame with reference line.	36
Figure 26. 2 nd left string motion magnification: (a) Original frame, (b) 40 times magnified frame, (c) magnified frame with reference line.	37
Figure 27. Side view of METU A1 Bridge (from East to West view).....	39
Figure 28. Side view drawing of METU A1 Bridge.....	40
Figure 29. Cross section of METU bridge before addition of billboards	41
Figure 30. Cross section of the bridge with additional billboards	42
Figure 31. Sketch of placement of accelerometer measurements	43
Figure 32. Frequency spectrum of 4 different measurements.....	43
Figure 33. FEM of the bridge.....	45
Figure 34. FEM of the tower of the bridge	46
Figure 35. FEM of the deck of the bridge.....	46
Figure 36. FEM of the cables of the bridge	47
Figure 37. FEM of the billboards on the bridge.....	48
Figure 38. First bending mode 2.63 Hz (left), first torsional mode 3.44 Hz (right) ..	50
Figure 39. Second bending mode 4.22 Hz: without billboards (left), with billboards (right)	51
Figure 40. Second torsional mode 4.35 Hz: without billboards (left), with billboards (right)	52
Figure 41. Third bending mode 6.60 Hz: without billboards (left), with billboards (right)	52
Figure 42. Fourth bending mode 8.40 Hz: without billboards (left), with billboards (right)	53
Figure 43. Power spectral density of phase measurements from video	55

Figure 44. Mode number vs. mode frequency graph of camera motion under influence of cable vibration (all peaks except 2.626 Hz and 2.854 Hz).....	56
Figure 45. 255 th frame original frame and magnified frame (2.6 - 2.7 Hz).....	57
Figure 46. 267 th frame with magnified frequency band 2.6 - 2.7 Hz	58
Figure 47. Sketch of placement of accelerometer measurements.....	69
Figure 48. Power spectral density of accelerometer measurements	70
Figure 49. Imaginary parts of Fourier transforms of 3 rd and 4 th readings	71
Figure 50. Zoomed power spectral density of accelerometer measurements	71

LIST OF ABBREVIATIONS

ABBREVIATIONS

1D	One Dimensional
2D	Two Dimensional
3D	Three Dimensional
ASCE	American Society of Civil Engineers
DSI	Devlet Su İşleri (General Directorate of State Hydraulic Works)
FEA	Finite Element Analysis
FEM	Finite Element Modeling
FFT & IFFT	Fast Fourier transform & Inverse Fast Fourier transform
FIR	Finite Impulse Response
fps	Frames per second
METU	Middle East Technical University
MIT	Massachusetts Institute of Technology
PSD	Power Spectral Density
RGB	Red Green Blue
SHM	Structural Health Monitoring
SNR	Signal to Noise Ratio

CHAPTER 1

INTRODUCTION

1.1. Importance of structural health monitoring (SHM)

Structural decay is a big problem faced by many developed countries in the world. After years of service, many structures, such as bridges, tunnels, dams, and power plants, are showing severe deterioration. The structural condition or “health” needs to be periodically monitored, in order to guarantee safety of these structures and to perform proper maintenance over time.

The main reason to apply SHM is to improve reliability of the existing structures. It is important that structures are designed to be cost effective and have long service of life. It is reported in ASCE infrastructure report card for year 2017 that almost 56000 bridges in USA, which is 10% of all existing bridges in the country, suffer from structural or functional deficiencies (ASCE, 2017). Such deficiencies require immediate attention, otherwise they may lead to serious damages. The dramatic example of Morandi Bridge in Italy shows that proper maintenance should be done at early stage of structural deficiency, before the damage occurs.

The Ponte Morandi, also known as Morandi Bridge, was a bridge engineered by Riccardo Morandi. It connected two districts across the Polcevera valley, Italy, and more importantly served as a link between Italy and France on European route E80. In August 2018, during the torrential rainstorm, 210 m section of the bridge collapsed, taking away 43 human lives. It is believed that collapse occurred due to structural weakness of the westernmost cable-stayed pillar of Ponte Morandi, where collapse was centered.

Therefore, proper SHM should be applied in order to improve reliability of the structure together with achieving lower cost condition maintenance, anticipating possible damage, and lastly but more importantly, avoiding catastrophic outcomes.

1.2. Modal identification as SHM method

One of the mostly used techniques for health monitoring and model characterization of the structure is dynamics-based vibration method, using modal identification (Shang & Shen, 2017). The main idea is that the damage and deterioration of the structure causes physical change in mass, damping, and stiffness which can be detected by measuring the abnormal responses of structural vibrations (Farrar & Jauregui, 1998).

Vibration measurements can be divided into two categories, contact and non-contact methods. The contact method involves wires and transducers, shown as small squares in Figure 1, that are located at a place of interest which allows to see the frequencies and amplitudes of vibrations. There is a variety of such contact transducers like accelerometers, linear variable displacement transducer, and strain gages. Although contact transducers can detect vibrations at long dynamic range and high accuracy, the physical installation is a costly, time and labor-consuming process and sometimes even impossible (Yang et al., 2017). Besides, the natural behavior of the structure may change with additional mass loading during inspection which is more profound for the structures of low mass (Nassif et al., 2005). This makes us question the practicability of these contact methods.

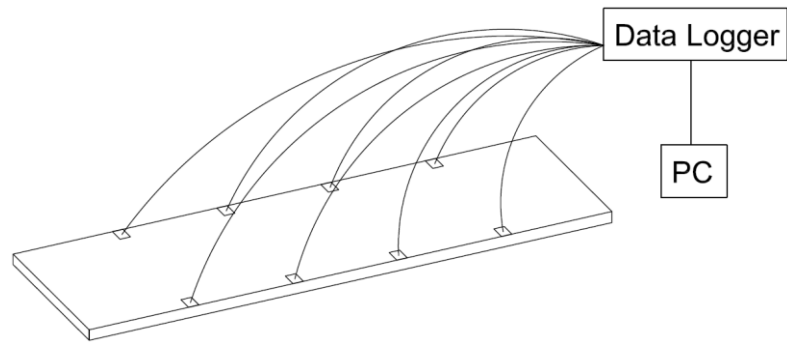


Figure 1. Contact method for vibration detection

More practical approach would be using non-contact measurement. At present, there are many different non-contact sensors such as Laser Doppler Vibrometry, synthetic aperture radar, ultra-sound systems, and vision systems.

The latter has several advantages over others in terms of cost and implementation (Baqersad et al., 2017). In addition, the robustness and accuracy of vision-based approach has been greatly enhanced with progress of image processing and computer algorithms (Baqersad et al., 2017). An excellent example for non-contact vision system is digital video camera, which are relatively not expensive and mobile. They can be effectively used for the vibration measurements of various structures when combined with suitable image processing algorithm (Caetano et al., 2011).

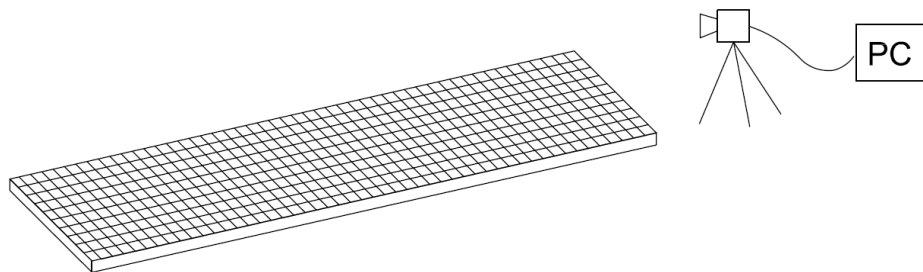


Figure 2. Video camera-based vibration detection

The main advantage of video-based method is that high spatial resolution can be obtained in a relatively efficient manner, since every pixel function as a separate sensor, as illustrated in Figure 2. On the other hand, in this method, high-contrast markers, which are placed on the surface of the structures are needed for point tracking. So, additional surface preparation is required, but it can be problematic when measurement area is large or inaccessible.

Camera-based measurements gained more wide acceptance with the development of motion magnification technique, which allowed video-based measurements without additional structural surface preparation. Besides, it became possible to have appropriate visualization of resonant vibration mode shapes without the use of paints and markers on the surface of the structure (Chen et al., 2015).

1.3. Motion microscopy

Motion detection is straightforward for video-based measurements when the displacement is large. However, for a tiny motion which is not detected by naked eye, the need for additional method arises. In analogy with daily life, where tiny living things are observed by the microscope, in the computer vision the imperceptible motions can be detected by the motion microscopy. The term motion microscopy was introduced by MIT researchers, Freeman and Rubinstein (2014). They described new method of motion magnification that enables us to amplify tiny motions in video in specified frequency band.

One of the most robust method for motion magnification is phase-based approach, which is described in more detailed manner in Chapter 2. Phase-based motion magnification approach has gained more attention recently due to wide range of possible applications. To illustrate, phase-based motion magnification can be used in pulse detection, sound detection from vibrating object, breath movement detection, etc.

Work done by Chen et al. (2015) can be given as in example for application of phase-based motion magnification in civil engineering. They have reported that by

using motion magnification algorithm together with phase-based motion estimation that resonant frequencies and operational deflection shapes can be detected. For their experiment they have used lab scaled benchmark structures like cantilever beam and pipe test specimen. They have showed that successful information about motion can be extracted from natural feature of the structure. Sarrafi et al. (2018) have reported application of phase-based motion magnification for determining resonant frequencies and operating deflection shapes of real-life sized wind turbine blade. In addition, they have used phase-based motion estimation to compare dynamic behavior of the structures from damaged and undamaged turbine blades.

Although there are many examples of various application of phase-based motion magnification, literature still lacks in infield measurements of structures under exploitation.

1.4. Aim of the study

Inspired by many successful applications of phase-based motion magnification in literature, the aim of this study is to utilize this method for the modal identification of METU A1 Bridge deck. The main objective of this research is to eliminate the use of expensive equipment. For that purpose, instead of expensive video camera simple and more available smartphone camera was used for all video recordings. Before applying current method to METU A1 Bridge, method was verified by experiments with METU A4 Bridge cable, ruler, and cello.

Within this thesis the phase-based motion magnification was utilized as a case study for modal identification of the bridge at outdoor condition. This method can be potentially used for modal identification of not only bridges but also large and complex structures where placing vibrational sensors is cumbersome.

CHAPTER 2

THEORETICAL BACKGROUND

In order to better understand working principle of phase-based motion magnification method, first, it is necessary to comprehend how the motion is detected.

2.1. Lagrangian and Eulerian approaches

In motion magnification just like in fluid mechanics, there are two different ways to track the motion, Lagrangian and Eulerian (Figure 3). The former describes the motion by tracking the specific object through space and time. The latter extracts the motion of an object by tracking the intensities of fixed pixels through the time.

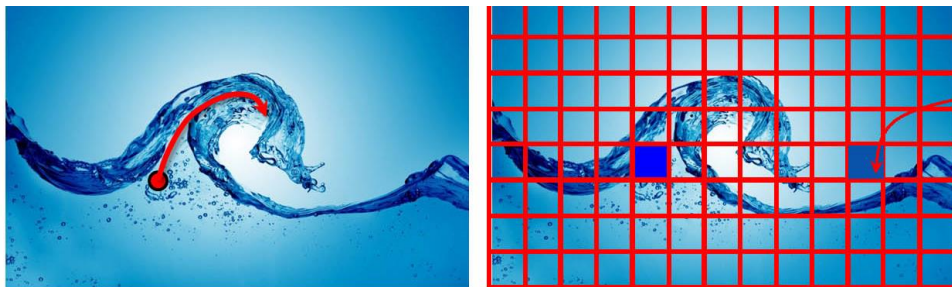


Figure 3. Lagrangian and Eulerian approaches (Rubinstein, 2014)

In other words, in Lagrangian approach pixels are separated to different groups where each group represent different tracking objects or segments, and only after that, the motion vectors can be amplified to reveal small motion. The major disadvantage of Lagrangian method is that after amplification of the motions it may leave black holes, which are needed to be filled with appropriate pixels (Figure 4). However, filling black pixels accurately has major difficulties.



Figure 4. Motion magnification by Lagrangian approach (Rubinstein, 2014)

The other method, Eulerian approach is more effective in terms of computational expense and robustness. In this approach, after amplification there is no need to fill the black pixels since it works in a different way. The intensities of each pixel are traced and then the motion is tracked by the help of signal processing. In addition, there is no need for segmentation since it tracks each pixel, which increases stability of process. These advantages gained Eulerian approach larger application.

2.2. Eulerian linear magnification

Initially, Eulerian linear magnification of intensity was used to amplify the temporal difference of the intensities of the pixels to observe the blood flow in the human body through the skin. It was seen that the amplification of temporal changes in intensities leads motion magnification spatially. In other words, the amplification of difference between brightness values of each pixel in time domain is directly proportional to magnification of translation of brightness values in space. This relation of intensities can be shown mathematically.

For the simplicity of understanding, lets first describe the process in one dimension. This description of the process is a review of Rubinstein work (2014) and derivations of the equations are taken from that work. If a single line of a video frame is taken, this line would have only intensity values in one spatial dimension. Then intensity values of translated signal can be written as $I(x, t)$, where x is position in

space and t is time. Intensity at time $t = 0$ can be expressed as $I(x, 0) = f(x)$. Then translated intensities can be written as

$$I(x, t) = f(x - \delta(t)) \quad \text{Eq. 1}$$

where $\delta(t)$ is time dependent displacement and at time $t = 0$ it is zero, $\delta(0) = 0$. Then the magnified translation, \hat{I} , can be expressed as

$$\hat{I}(x, t) = f(x - (1 + \alpha)\delta(t)) \quad \text{Eq. 2}$$

where α is a magnification factor.

In order to magnify intensity, firstly, change in intensity between $t=0$ and $t=t$ should be derived. The change in the intensity, B , with respect to the $I(x, 0)$ is

$$B(x, t) = I(x, t) - I(x, 0) \quad \text{Eq. 3}$$

By using first-order Taylor series expansion about x and assuming that $\delta(t)$ is respectively small, $I(x, t)$ in Eq. 1 can be approximated as

$$I(x, t) \approx f(x) - \delta(t) \frac{\partial f(x)}{\partial x} \quad \text{Eq. 4}$$

Derived change in intensity, B , can be approximated as

$$B(x, t) \approx -\delta(t) \frac{\partial f(x)}{\partial x} \quad \text{Eq. 5}$$

Amplification in intensity between $t = 0$ and $t = t$ can be written as

$$\hat{I}(x, t) = I(x, t) + \alpha B(x, t) \quad \text{Eq. 6}$$

Combining equations Eq.4, Eq.5, and Eq.6 gives approximated magnified intensity in terms of α and $\delta(t)$

$$\hat{I}(x, t) \approx f(x) - (1 + \alpha)\delta(t) \frac{\partial f(x)}{\partial x} \quad \text{Eq. 7}$$

Assuming that translation of intensities and its magnification $(1 + \alpha)\delta(t)$ is not too large, it is possible to take another first-order Taylor approximation to magnified intensity in Eq. 7 to give Eq.8

$$\hat{I}(x, t) \approx f(x) - (1 + \alpha)\delta(t) \quad \text{Eq. 8}$$

Comparing Eq. 1, which expresses motion magnification and Eq. 8, which is approximation for intensity magnification, it can be seen that these two magnifications are roughly equal.

Figure 5 graphically shows that magnifying intensity linearly between time 0 and t , magnifies motion linearly as well. In other words, linear approximation between actual and magnified motions is produced.

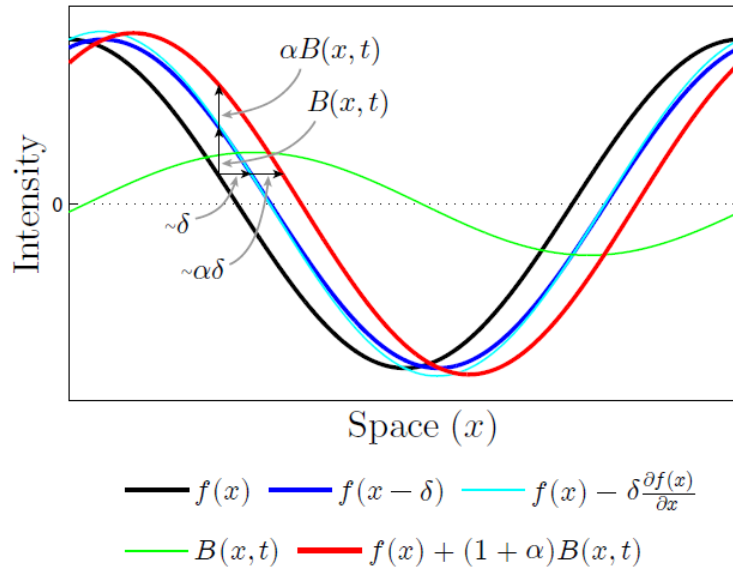


Figure 5. Motion magnification with linear approximation (Rubinstein, 2014)

The major setback of this method is that large linear amplification in intensity values gives unclear results in reconstructed video, due to increase in noise power. To increase the signal to noise ratio, instead of linear amplification the alternative method

of phase-based motion magnification can be used which amplifies phase differences of the intensity values. The difference between result of two methods demonstrated in Figure 6, where (a) is an input noise, (b) is linearly magnified, and (c) is result of phase-based magnification.

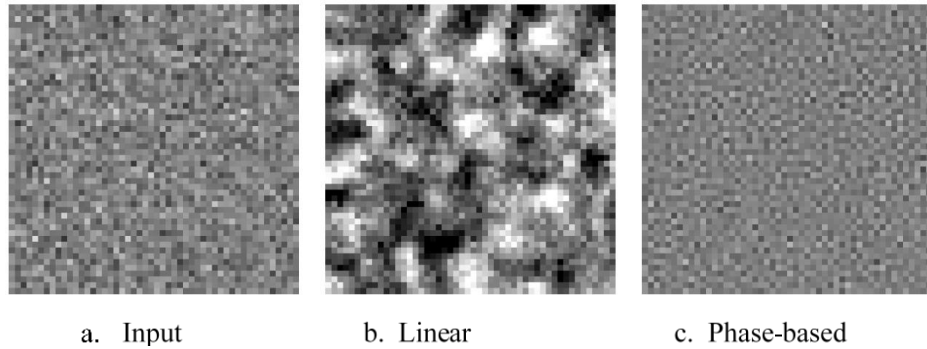


Figure 6. Magnified noise of Linear magnification and Phase-based magnification (Wadhwa, 2016)

2.3. Phase-based motion magnification

In order to better comprehend the phase-based motion amplification, a better understanding of term phase is needed.

2.3.1. Definition of phase

Colorful image or RGB video frame can be transformed to the grayscale image and image would be represented in intensity values of whiteness. Moreover, image can be further transformed from spatial domain to the frequency domain with Fourier transformation method. Fourier transformation represents a signal in terms of its basis functions. Basis functions has different form such as standard form $\{\sin(\omega t), \cos(\omega t), \omega \in \mathbb{R}\}$ and exponential form $\{e^{-i\omega t}, \omega \in \mathbb{R}\}$ where ω is frequency. Taking a Fourier transformation of a signal or function $f(x)$ in space domain gives us complex form of representation in frequency domain

$$\mathcal{F}(f(x)) = F(\omega) = \int f(x)e^{-i\omega x} dx = a(\omega) + ib(\omega) \quad \text{Eq. 9}$$

where a and b are some real numbers.

Complex form can be also expressed in polar coordinates

$$a(\omega) + ib(\omega) = |F(\omega)|e^{i\phi(\omega)} = \sum_{\omega} A_{\omega}e^{i\phi_{\omega}} \quad \text{Eq. 10}$$

where $\phi(\omega)$ is called phase angle, A_{ω} is called amplitude and equals to $A_{\omega} = |F(\omega)| = \sqrt{a^2 + b^2}$, Figure 7.

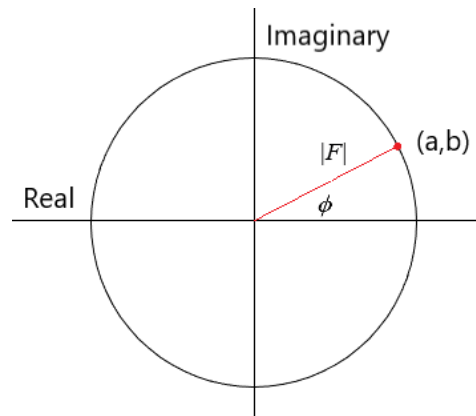


Figure 7. Phase representation in complex domain

Phase is playing big role in construction of image. The simple example of phase domination can be seen in Figure 8, where amplitudes and phases swap between two pictures are shown.

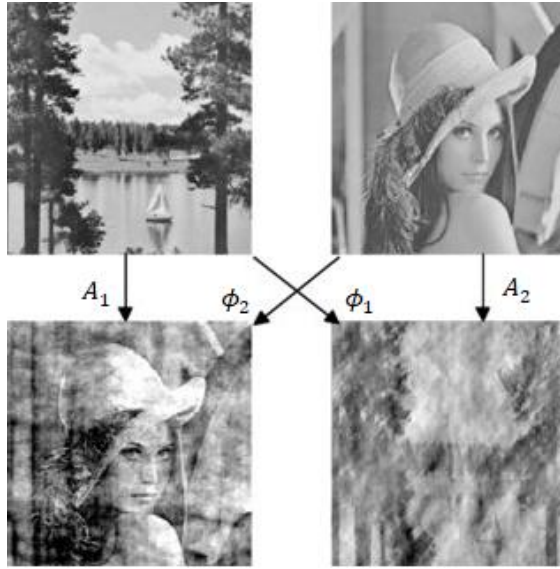


Figure 8. Swap of amplitudes and phases of two different pictures (Skurowski & Gruca, 2009)

From Figure 8 it can be seen that when two pictures are swapped the contours of image that was selected as phase component is more dominant than the ones which was selected as amplitude component.

2.3.2. Global magnification of motion

To get one step closer to local phase-based motion magnification, it is helpful to describe global case.

As it was mentioned before, $I(x, t)$ is intensity values of 1D image signal and equals to $f(x - \delta(t))$, where δ is translation distance and $\delta(0) = 0$. The Fourier shift theorem states that translation of a signal in space can be represented in Fourier domain by multiplication of $e^{-i\omega x}$ to its Fourier transform, where x is translation distance in space domain. Treating intensity signal by Fourier transformation gives the collection of amplitudes and phases

$$\mathcal{F}(f(x)) = \sum_{\omega} A_{\omega} e^{i\phi_{\omega}} \quad \text{Eq. 11}$$

Therefore, translated intensity $I(x, t)$ can be represented as

$$\mathcal{F}(f(x - \delta(t))) = \sum_{\omega} A_{\omega} e^{i\phi_{\omega}} e^{-i\omega\delta(t)} = \sum_{\omega} A_{\omega} e^{i(\phi_{\omega} - \omega\delta(t))} \quad \text{Eq. 12}$$

The linearity of Fourier transform allows extraction of phase difference between $t=0$ and $t=t$ phases

$$I(x, t) - I(x, 0) = \mathcal{F}^{-1} \left[\sum_{\omega} A_{\omega} e^{i(\phi_{\omega} - \omega\delta(t))} - \sum_{\omega} A_{\omega} e^{i\phi_{\omega}} \right] = \mathcal{F}^{-1} \sum_{\omega} A_{\omega} e^{-i\omega\delta(t)}$$

Eq. 13

After phase difference $\omega\delta(t)$ is extracted, which is directly proportional to translation, the motion can be magnified by factor of α

$$\hat{I}(x, t) = f(x - (1 + \alpha)\delta(t)) = \mathcal{F}^{-1} \left[\sum_{\omega} A_{\omega} e^{i(\phi_{\omega} - (1+\alpha)\omega\delta(t))} \right] \quad \text{Eq. 14}$$

(Wadhwa, 2016)

By using Fourier transform theorem magnified global motion can be easily achieved. However, in real life the objects in videos do not move globally, on the contrary, they move separately, i.e. locally. Local movement can be seen even at different parts of the same object. Thus, images need to be decomposed to local basis function where phases of local motion can be tracked. For that purpose, complex steerable pyramid is utilized, which uses local waves (wavelets) as a basis function for tracking local motions.

2.3.3. Complex steerable pyramid

Complex steerable pyramid is an overcomplete linear transform. Overcompleteness is concept from linear algebra where removal of one element from subset of a system, does not result in completeness of the system. Pyramid in image processing is a representation of a signal or an image in multiple scales where graphical representation of the process looks like pyramid. There are two types of pyramid low pass and band pass pyramids. Low pass pyramid usually used for

smoothing sharp images by using averaging filter. Band pass pyramid is used for decomposition of image to different levels, where each level achieved by applying different bandpass filters. In complex steerable pyramid the band pass pyramid method is used to decompose the image into different scales and orientations with the help of bank of steerable filters. This representation of image in coefficients of steerable filters allows to track local motion, since steerable filters work as 2D wavelets for 2D images.

2.3.3.1. Local motion magnification of 1D image

Before applying complex steerable pyramid to 2D image it is easier to comprehend its working principle by describing local motion magnification in 1D, since working principles of the steerable filters in 1D and 2D are similar.

Consider 1D image having only intensity values. In this case, to track local phases 1D signal is decomposed into sets of wavelets, which are localized infinite complex sinusoids. In order to localize complex sinusoids represented as $e^{i\omega x}$, Gaussian window function $e^{\frac{-x^2}{2\sigma^2}}$ is used. Consequently, resultant wavelet is described as $e^{\frac{-x^2}{2\sigma^2}}e^{i\omega x}$. Graphical illustration for this process is shown in Figure 9.

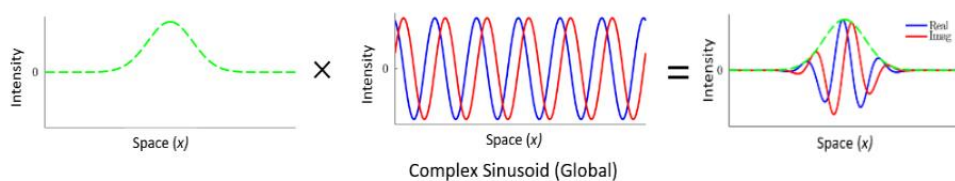


Figure 9. Gaussian windowing of complex sinusoid (Wadhwa, 2016)

Since basis functions of complex steerable pyramid are self-similar the ratio between standard deviation σ of Gaussian window and frequency of complex sinusoid

ω is fixed. In other words, to obtain similar wavelets Gaussian window can deviate so that σ/ω is constant.

In order to translate 1D signal by distance of $\delta(t)$, where $\delta(t) = \frac{\phi}{\omega}$, the phase of wavelet is shifted, which is done by multiplying the wavelet function with $e^{i\phi}$

$$e^{\frac{-x^2}{2\sigma^2}} e^{i\omega x} e^{i\phi} = e^{\frac{-x^2}{2\sigma^2}} e^{i\omega(x + \frac{\phi}{\omega})} = e^{\frac{-x^2}{2\sigma^2}} e^{i\omega(x + \delta)} \quad \text{Eq. 15}$$

(Wadhwa, 2016)

and phase difference between shifted and not shifted wavelet is equals to $\omega\delta$ which is proportional to local motion.

Figure 10 illustrates how local motion in original signal effects composition of wavelets where only related wavelet response to the local motion.

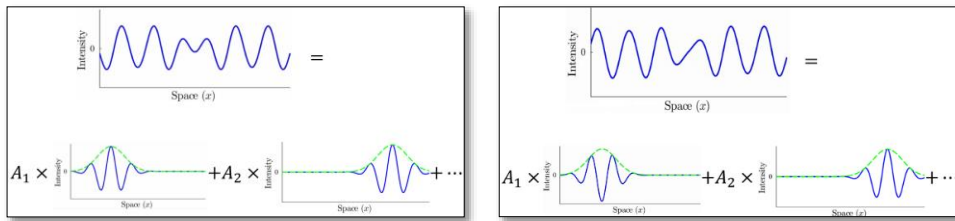


Figure 10. Decomposition of the signal into wavelets (Wadhwa, 2016)

After phase difference is derived, it can be magnified by factor of α to synthesize local motion magnification which is represented by

$$e^{\frac{-x^2}{2\sigma^2}} e^{i\omega(x + (1 + \alpha)\delta)}$$

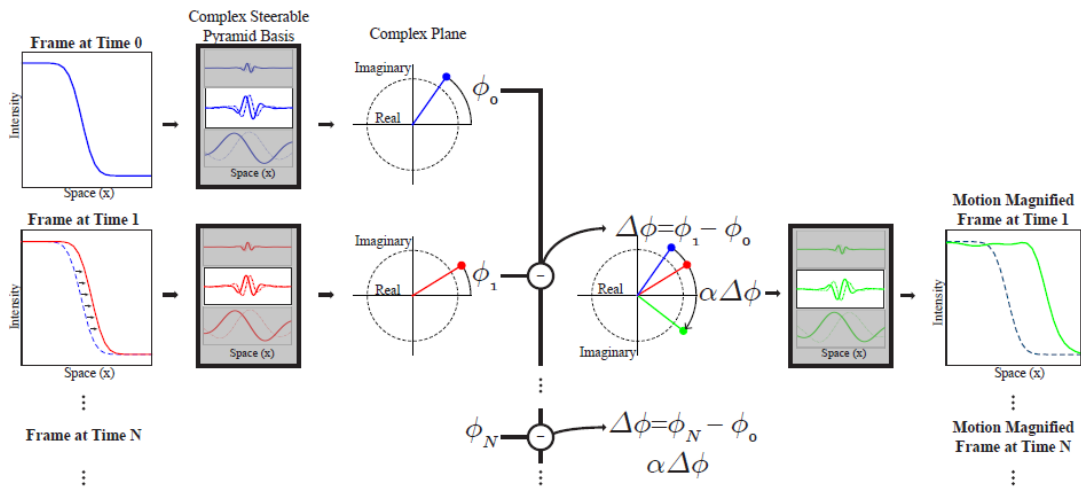


Figure 11 Motion magnification of 1D signal (Wadhwa, 2016)

Figure 11 shows the graphical illustration of overall process how motion is magnified using complex steerable filter in 1D. In Figure 11 input signal at $t=0$ is represented by blue color and signal frame at $t=1$ is shown in red. When complex steerable pyramid basis is applied to each frame separately the signals are decomposed into sets of wavelets. Respective wavelets of same frequency are chosen, and resultant phases are shown in complex plain in Figure 11. The difference between phases is calculated and multiplied by α to give magnified motion which is shown in green color. Reconstruction of resultant shifted wavelet clearly shows that the motion in frame at $t=1$ was magnified.

In Figure 11 the amplification of motion by using single element of basis function is illustrated. However, when signal is decomposed into complex steerable pyramid basis there are multiple number of elements. Described process is applied to all of the elements in the same way. Then the combination of these elements gives magnified local motions.

2.3.3.2. Motion magnification of 2D image

When all operations are considered in two dimensions, number of components of basis function increases by number of orientations.

Application of complex steerable filter bank to each frame of the video, gives amplitude and phase values for each pixel of frame. These values are different for each scale ω (texture frequency) and orientation θ .

Mathematical representation of extraction of amplitude, $A_{\omega,\theta}$, and phase, $\phi_{\omega,\theta}$, values from each frame using complex steerable filters is shown in Eq. 16.

$$A_{\omega,\theta}(x, y, t_0)e^{i\phi_{\omega,\theta}(x,y,t_0)} = I(x, y, t_0) \Psi_{\omega,\theta} \quad \text{Eq. 16}$$

(Wadhwa, 2016)

Here $\Psi_{\omega,\theta}$ is complex steerable filter or 2D wavelet which differs by scale and orientation.

Decomposition of the frames according to scale, orientation, and position is done in Fourier domain. Therefore, filters and frames need to be transferred to frequency domain.

Figure 12 shows complex steerable filters of different scales and orientations in space domain, Figure 12a, and frequency domain, Figure 12b. 2D filter in frequency domain can be also illustrated in 3D, Figure 12c. In Figure 12d idealized filter map is illustrated where each filter is shown in different distinctive color and each filter covers related area. On this map one can also see high and low pass filters which are not involved in magnification. Since, the basis function is complex the map shows only real part and imaginary part is represented in black color.

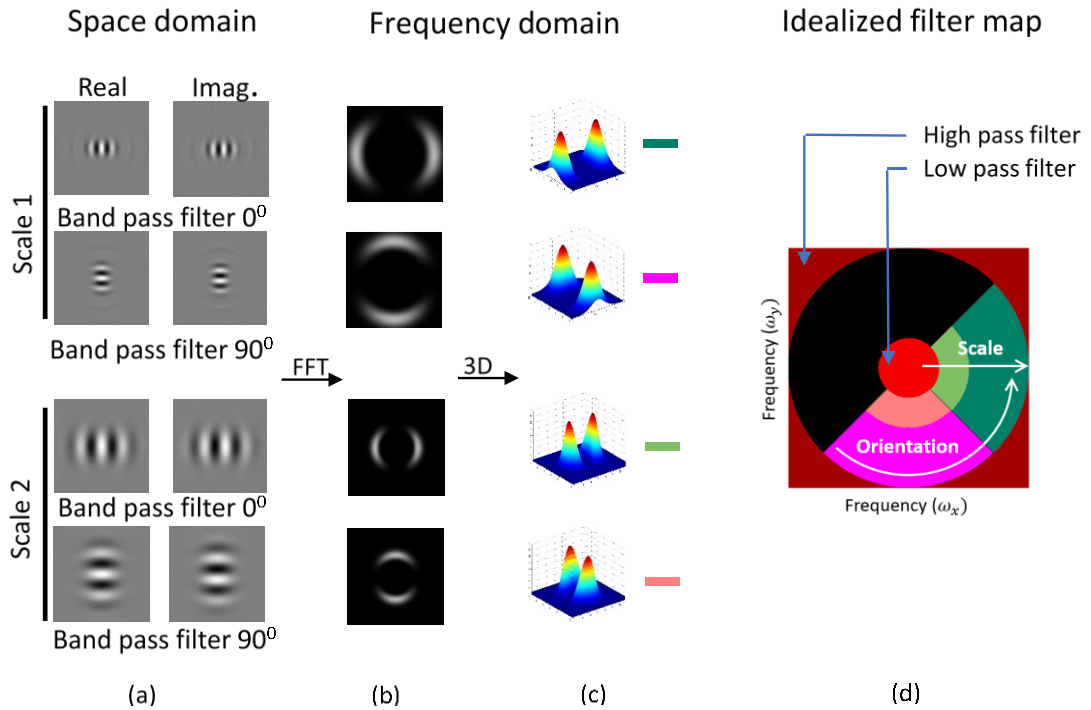


Figure 12. Complex steerable filters (Wadhwa, 2016)

Figure 13 explicitly shows working flow of phase-based motion magnification. Initially input video is transferred to frequency domain using Fast Fourier Transform, Figure 13, step (1). Then the images in frequency domain pass through sub band filters of the complex steerable pyramid basis. Sub band are sorted into three categories: high pass, band pass, and low pass Figure 13, step (2). High pass and low pass filters correspond to high and low texture frequencies that are not in range of interest, hence, directly added to final reconstructed video. Frames from the video in frequency domain filtered by band pass filters of different scales and orientations, results are operated by IFFT to extract amplitudes and phases of the frames Figure 13, step (3). In order to attenuate unwanted frequencies of phases in time domain and magnify target frequencies, temporal filter, FIR, is applied Figure 13, step (4). Finally, resultant phases are multiplied by magnification factor of α , Figure 13, step (5), and motion magnified video is reconstructed, Figure 13, step (6).

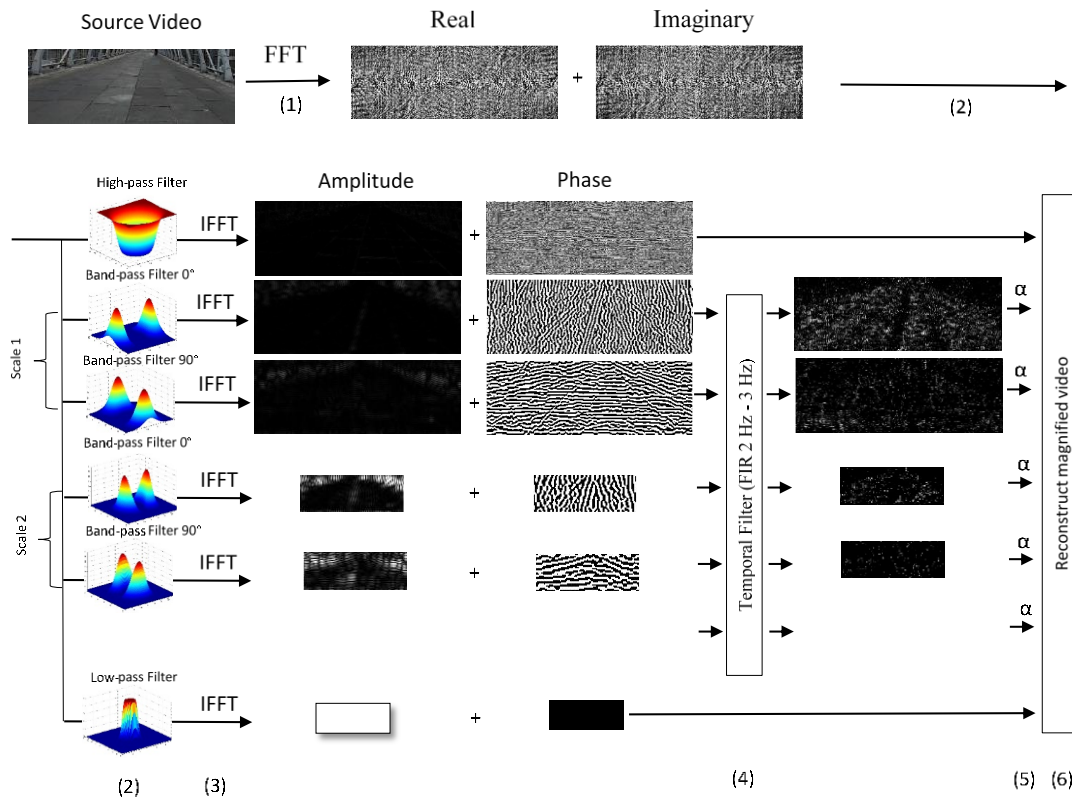


Figure 13. Work flow of motion magnification

This method can be used not only for motion magnification but also for motion estimation by applying modifications in source code (Wadhwa, 2013). Modified code takes first 3 steps of the work flow, described in Figure 13, and adds operations on phase values of the frames to extract vibrational frequency spectrum of target region. Since phase is directly proportional to translation, frequency spectrum can be extracted for each scale by treating phase difference as spatial displacement. In other word, after step (3) in Figure 13, without applying remaining steps, phase values of each pixel can be transferred to frequencies domain to extract frequency spectrum of phase change in time domain. By this way, frequency spectrum of a single pixel or an average of frequency spectra of target region pixels can be achieved. Averaging can be done with amplitude weighted, where pixels with higher amplitude are more valued. In other words, pixels with good texture are assigned more weight. The

another of achieving averaged frequency spectrum is not by averaging spectra of pixels but by averaging phases of each frame of target region and then transferring it to frequency domain.

2.3.3.3. Types and bounds of complex steerable filters

There are different types of complex steerable filters which vary in terms of scale, orientation, and bandwidth. All filters mentioned before have octave bandwidth, Figure 14a. Unlike Figure 12d, in Figure 14a the number of orientations is increased from 2 to 4, and the number of scales is increased from 2 to 3.

Magnification of motion cannot be done infinitely. The limits for magnification are restricted by bounds of the steerable filters. The bound of octave bandwidth filter is introduced as $\alpha\delta(t) < \sigma$, where α is magnification factor, $\delta(t)$ is displacement of motion and σ is standard deviation of the Gaussian window. Standard deviation can be approximated to $4\sigma \approx \lambda$, where λ is special wavelength of sinusoid under Gaussian window. Thus,

$$\alpha < \frac{\lambda}{4\delta(t)} \quad \text{Eq. 17}$$

However, for half-octave and quarter-octave bandwidth filters λ is 2 time and 4 time smaller than for octave bandwidth filter, Figure 14b and Figure 14c. Therefore, for half-octave filter α is bounded as

$$\alpha < \frac{\lambda}{2\delta(t)} \quad \text{Eq. 18}$$

and for quarter-octave filter as

$$\alpha < \frac{\lambda}{\delta(t)} \quad \text{Eq. 19}$$

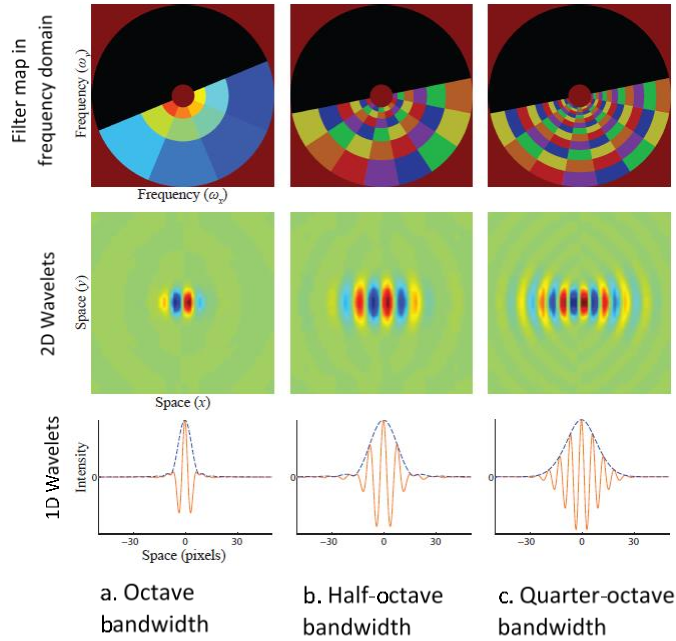


Figure 14. Types of complex steerable filters (Wadhwa, 2016)

From the equations Eq. 17, Eq. 18, and Eq. 19 it is understood that using sub-octave bandwidth filters is more beneficial. Nevertheless, it has a major disadvantage, which is computational expense, in terms of memory and time of processing.

2.3.4. Limitations of phase-based motion magnification

Although phase-based motion magnification overcomes the problem with signal to noise ratio and higher magnification can be achieved compared to linear magnification, there are still several limitations of this method.

A major limitation is the light. It is extremely important to have constant illumination, otherwise the local phases would be interpreted in a wrong manner. This limitation is mostly valid for the lights which are powered by alternative current. To solve this constraint, constant light that does not flicker can be used. For the outdoor video captures clouds may lead to changes in lighting, but if the motion of clouds is slow, the effect of the change in lighting may not impact the extracting local phases.

Another important limitation is the camera motion. If the camera is placed on the vibrating base the motion identification can be misinterpreted. This is not valid for the motions of a lower frequencies like accidental shake of hands. Unless, this motion is being magnified intentionally.

One other restraint is the texture. In order to detect the motion enough visual contrast is required. If the computer program cannot detect the edges of the object, then the motion would stay unrevealed.

The motion displacement is also an important limitation for phase-based motion magnification. For an efficient amplification motion displacement should be in range of one pixel or smaller. To get around this limit, one can downsample the size of the video which would result in merging of the pixels. Consequently, large motions can be shrunk to face the requirement of the small motion in the range of one pixel or smaller. Besides, downsampling decreases the size of the video which is helpful in reducing processing time.

CHAPTER 3

EXPERIMENTAL RESULTS

3.1. Method verification

Before applying phase-based motion magnification in the modal identification of the METU A1 Bridge, firstly, method was verified on several simple experiments. The method verification was firstly performed on bridge cable, ruler, and cello to ensure that theoretical and experimentally obtained magnified resonant vibration shapes match.

3.1.1. METU A4 Bridge cable experiment

To begin with, vibrations of cables for METU A4 pedestrian bridge were identified. For that, the video of excited cables of the bridge was captured from the side view on the smartphone camera. The video from smartphone was processed with help of existing algorithms. The range of the video from 1 to 24 Hz was magnified by iteration 23 times, with interval of 1 Hz. It was observed that at constant interval of 4 Hz the shape of the cable changes, which is true only for certain frequency bands. Figure 15 visualizes first five vibrational modes of the cable that were seen upon amplification in a magnitude of 100 times. First modal shape of the cable was observed in 3-4 Hz band, Figure 15b, and in interval of 4 Hz, i.e. 7-8 Hz second modal shape was seen, Figure 15c. Similarly, third and fourth bands were observed within constant interval in 11-12 Hz and 15-16 Hz, respectively, Figure 15d and Figure 15e. Small deviation in interval between fourth and fifth modal frequencies was seen, and fifth modal shape was observed in 21-22 Hz band, Figure 15f. This deviation could be as result of the contact between cable and handrail.

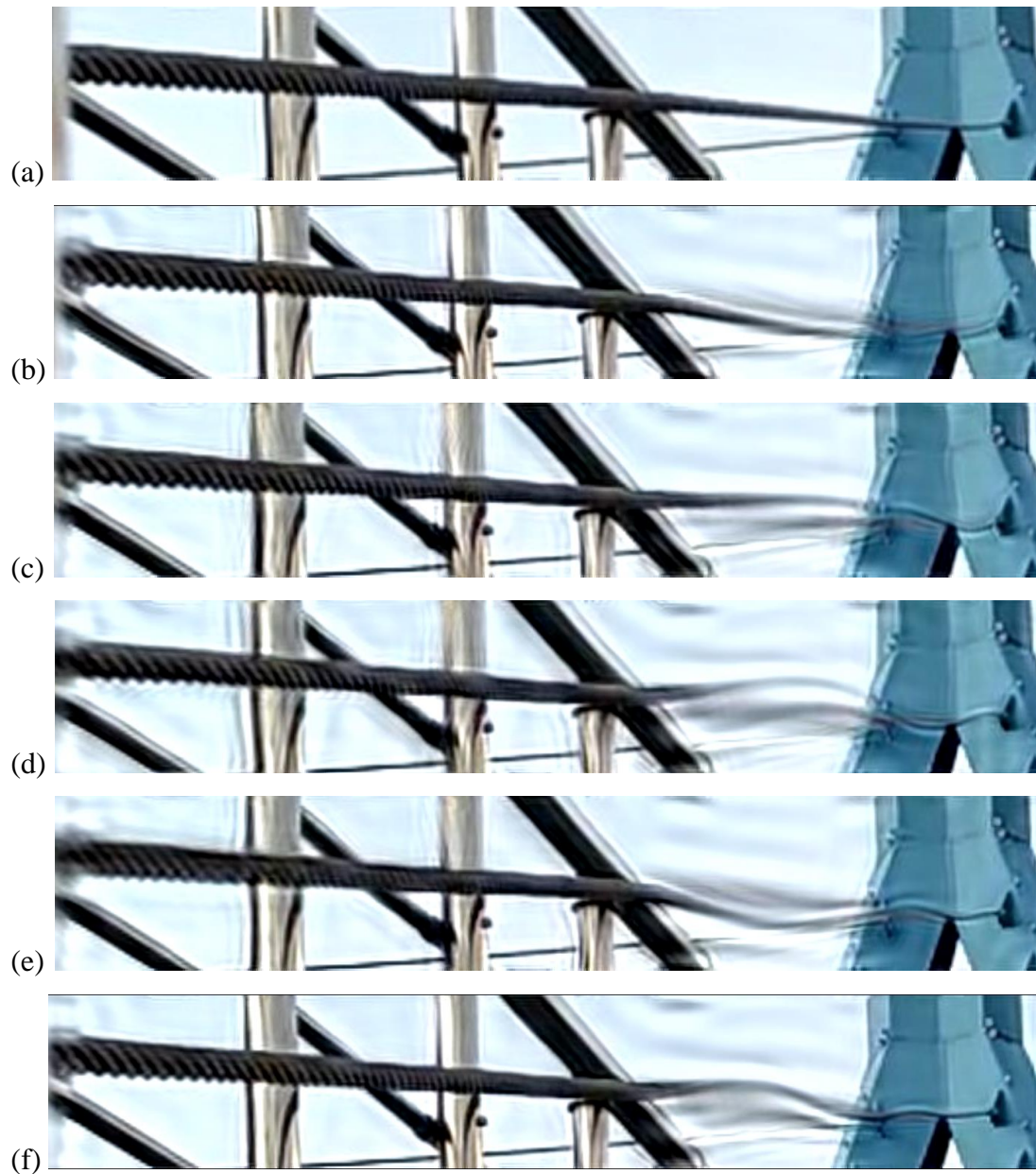


Figure 15. (a) Original frame. Magnified 100 times mode shapes of the cable: (b) first, (c) second, (d) third, (e) fourth, (f) fifth.

From the Figure 15 it is possible to see that the shapes of the vibrational modes of the cable can be seen with naked eyes.

In theory the interval of modal frequencies of cable is constant. Therefore, constant interval between modal frequencies retrieved by motion magnification gives this method big chances that current method works properly. From the mode number verses mode frequency graph (Figure 16) it can be seen that the $R^2 \approx 1$, which means that the values found experimentally are theoretically true, since the natural vibration frequencies of a cable have linear relation to mode numbers. This relation is shown in Equation 20 (Lee & Chen, 2004),

$$f_n = \frac{n}{2L} \sqrt{\frac{T}{m}} \quad \text{Eq. 20}$$

where n is vibration mode, L is length of the cable, T is axial load in the cable, m is mass of the cable. Since length, axial load and mass of the cable is constant for certain cable, the mode frequency changes depending only on change in mode number.

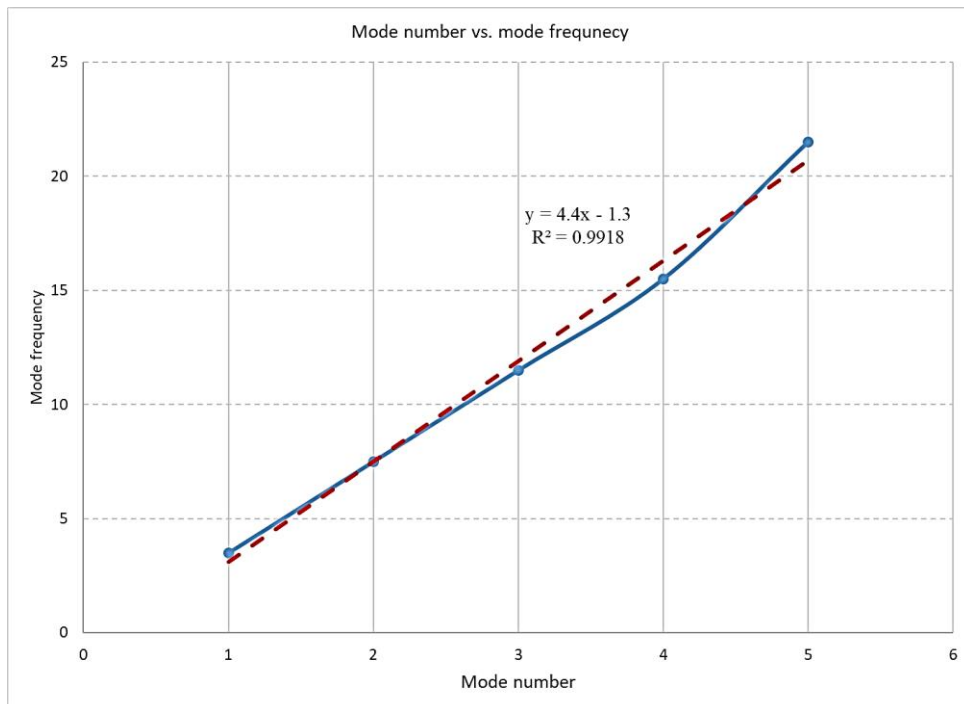


Figure 16. Mode frequencies of cable

After successful application of phase-based motion magnification algorithms on bridge cable and visually determining vibrational mode shapes, experiments on simple object were done. Modal frequencies of simple object like ruler and cello were extracted using phase-based motion magnification, besides modes were also calculated analytically and two results were quantitatively compared. In these experiments in addition to currently existing method new modifications to the algorithm were developed. By using modified algorithm, instead of searching for motion in magnified video manually, it became possible for the software to screen videos and find magnified motions automatically.

3.1.2. Ruler experiment

For the ruler experiment steel ruler with 94x4x0.1 cm dimension was used, where 6 cm fixing part is not included (Figure 17a). The smartphone was used as accelerometer, for that “Accelerometer Meter (version 1.32)” application was used (Keuwlsoft 2015). Only out of plane acceleration of the smartphone was taken into account. The frequency limit for smartphone accelerometer is 200 Hz. The phone was placed between 65 cm and 80 cm from the top of the ruler, as shown in the Figure 17b.



Figure 17. Fixing point of the ruler

The ruler was excited by hitting to the bottom of the ruler, below the phone, with steel hammer. The measurement from accelerometer showed first three vibrational modes to be 0.7509 Hz, 4.702 Hz, and 12.95 Hz, as shown in the frequency spectrum in Figure 18. The accelerometer recorded 82 seconds of vibration, so the sampling rate is 0.012 Hz.

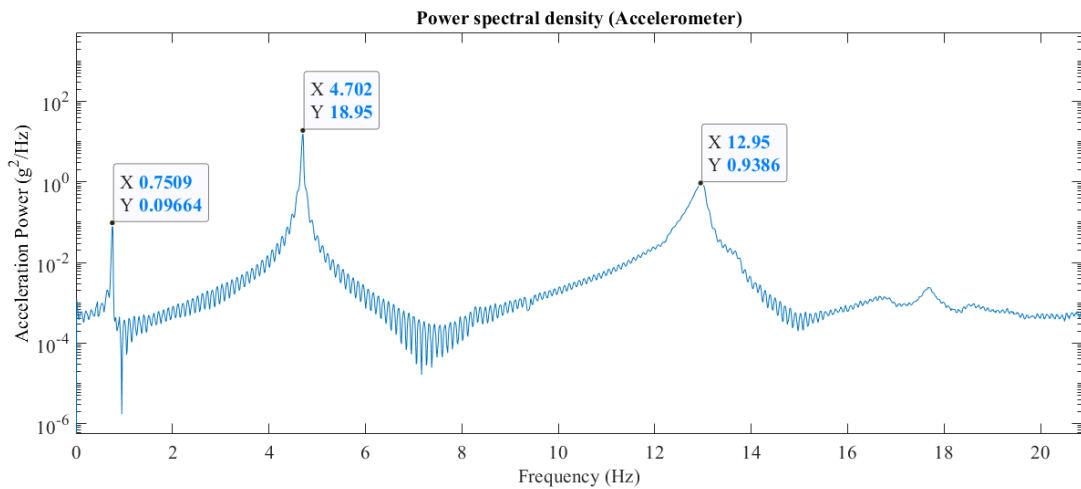


Figure 18. Power spectral density of smartphone accelerometer measurement

For the phase-based motion estimation of the excited ruler video, the video was taken by using simple smartphone with 30 fps and 1920x1080 frame dimensions. The camera was fixed on tripod and placed approximately at half-meter distance. While processing, to avoid noise and to reduce processing time video frames were cropped at the region of interest. All the processing was done by MATLAB software program and modified phase-based motion magnification algorithm.

After screening many literature examples and extensively studying existing algorithm, it was possible to extract phases from input video and obtain the frequency spectrum of the motion. Resulted frequency power spectrum density of the video is illustrated in Figure 19. Spectrum was taken by averaging phase of each frame. As can

be seen from the Figure 19, strong peaks at 0.7531 Hz and 4.699 Hz represent first and second bending modes of the ruler, which are compared to ones that are found by using accelerometer.

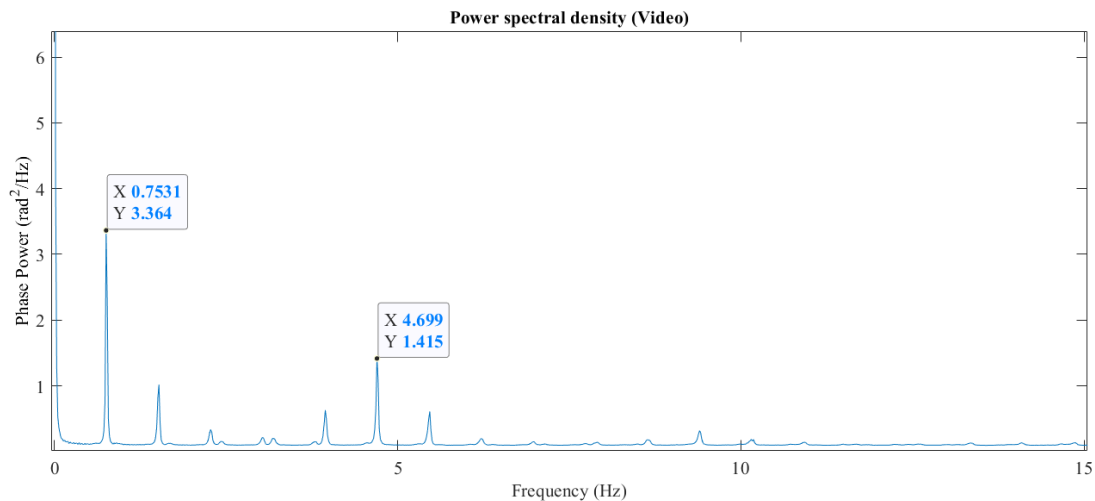


Figure 19. Power spectral density of phase measurement from video

Placing the smartphone on the ruler causes additional damping, which significantly decreased third mode. In order to observe third mode of the ruler, first 5 seconds of the video of excited ruler were taken. The spectrum extracted from 5 second video is shown in the Figure 20. As it can be seen from the spectrum, a small peak with borders at 12.92 Hz and 13.11 Hz can be observed that is averaged to 13.02 Hz. This proves that third mode can be captured on the first five seconds of the video before it attenuates.

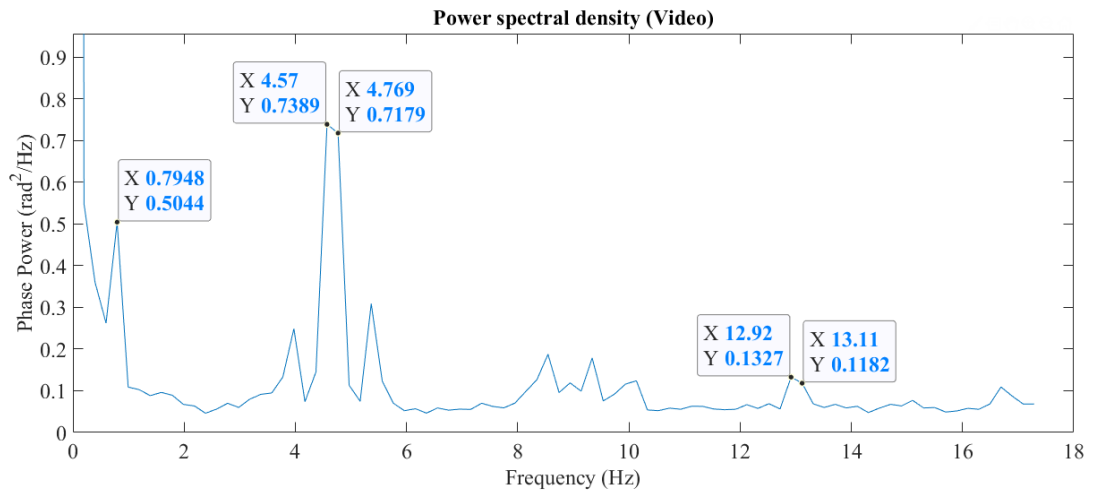


Figure 20. Power spectral density of phase measurement from 5 seconds video

There are small peaks on frequency spectra on Figure 19 and Figure 20 which were disregarded due to two main reasons. The first reason is that the surface of steel ruler is smooth and shiny, therefore, due to presence of bright light it glitters. Glittering is one of the limitations of the phase-based magnification method that was discussed in Chapter 2. The other reason for having such noise might be software related. After observing same pattern in frequency spectrum of bridge deck (Section 4.4.1) it was considered that algorithm might have produced some artefact of first resonant mode that repeats itself with constant intervals.

Table 1. Table of comparison of theoretical and experimental results

Mode numbers	Accelerometer measurements (Hz)	Video measurements (Hz)	Sampling rate of the spectrum of the video (Hz)	Error (%)
1	0.7509	0.7531	0.016	0.293
2	4.702	4.699	0.016	0.0638
3	12.95	13.02	0.199	0.541

As can be seen from Table 1, the error between vibrational modes extracted from the video and actual values reported by accelerometer are 0.293%, 0.0638%, and 0.541% for first, second and third vibrational modes, respectively. It can be concluded that all three mode frequencies of video measurement are well precise to the accelerometer data and lies within the sampling rate region. Such small error verifies applicability of the phase-based method in the outdoor use.

3.1.3. Cello experiment

For the cello experiment smartphone camera with ability to capture 240 frames per second was used. Left two strings of the cello were calibrated to 65.4 Hz and 98.0 Hz. Unlike ruler experiment for the cello experiment, camera was not stabilized by using tripod but it was stabilized by hand only.

For the video recordings Samsung Galaxy S7 Edge smartphone was used, and videos were captured at slow-motion mode to achieve frame rate of 240 fps as indicated in phone characteristics. However, details of the captured video showed that frame rate varies for each recording. The numerical values for two measurements for each string are shown in the Table 2. As it can be seen, the actual number of frames per second in the captured video is different for every recording (Table 2, entry 3), and the extracted first vibrational mode shows large deviation from the true value (Table 2, entry 4). However, when frame rate is adjusted to 240 fps the first mode frequencies extracted for each string are in agreement with calibrated frequencies (Table 2, entry 7).

Table 2. Data extracted from the cello videos

1	String No.	1st left string		2nd left string	
2	Video No.	1	2	3	4
3	Indicated fps	192	202	181	173
4	1st mode frequency (Hz)	52.5	55.1	74.0	70.5
5	Sampling rate (Hz)	0.09	0.05	0.07	0.07
6	Modified to 240 fps	240	240	240	240
7	1st mode frequency (Hz)	65.4	65.6	97.3	97.3
8	Sampling rate (Hz)	0.12	0.06	0.09	0.09
9	Error % between modified & calibrated	0.00	0.31	0.71	0.71

The frequency spectrum extracted from the Video-1 before frame rate adjustment is given in Figure 21. Since the top of the peak was not sharp, it was hard to determine its exact position, therefore, frequency mode of 52.5 Hz was determined by averaging peak borders, 50.9 Hz and 54.1 Hz.

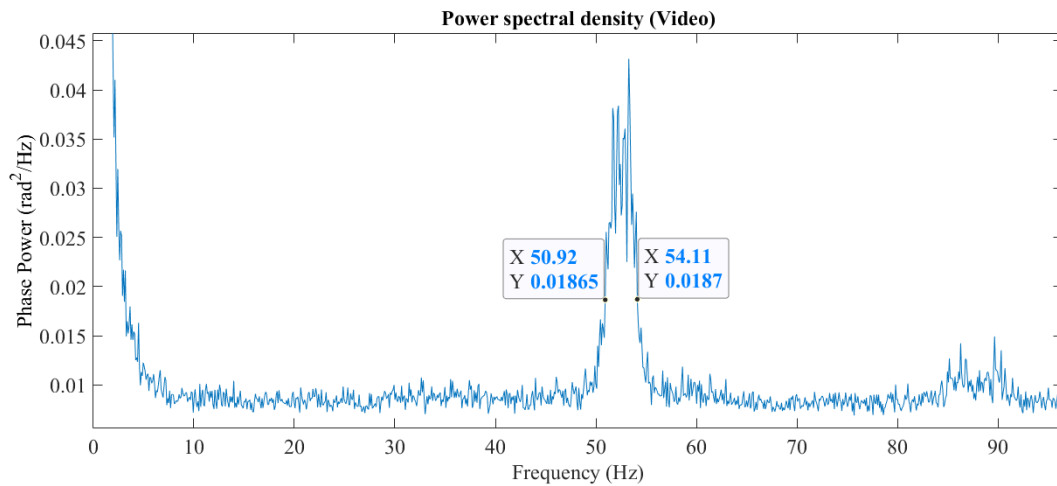


Figure 21. Power spectral density of phase measurement from 1st left string excited Video-1, without frame rate adjustment

The frequency spectrum extracted from Video-1 after adjustment of frame rate to 240 fps is shown in Figure 22. Averaging the peak borders 63.5 Hz and 67.4 Hz, resulted as 65.4 Hz, which matches the calibrated value of the 1st left string.

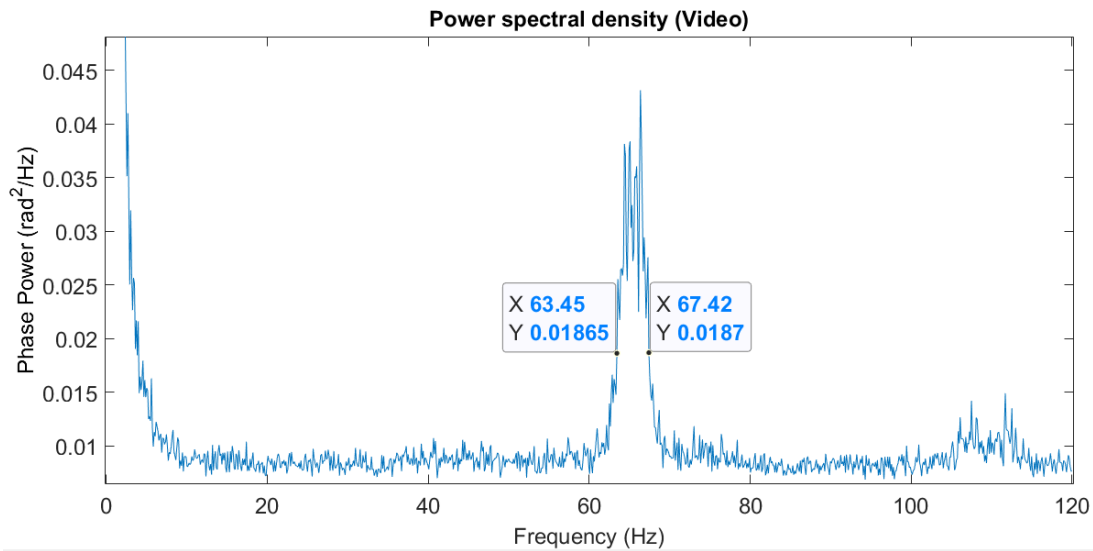


Figure 22. Power spectral density of phase measurement from 1st left string excited Video-1, with frame rate adjustment to 240 fps

Figure 23 shows the frequency spectrum extracted from Video-4 with frame rate 173 fps. Spectrum shows that at such frame rate the first vibrational mode of 2nd left string is 70.5 Hz.

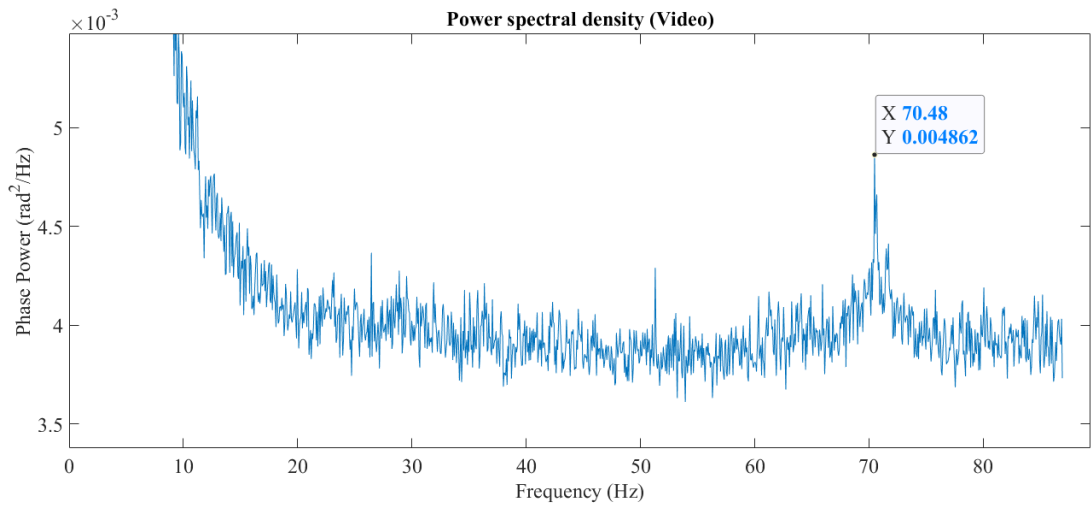


Figure 23. Power spectral density of phase measurement from 2nd left string excited Video-4, without frame rate adjustment

However, when the frame rate of Video-4 was adjusted to 240 fps, the frequency mode changed to 97.3 Hz (Figure 24) which is closer to calibrated value.

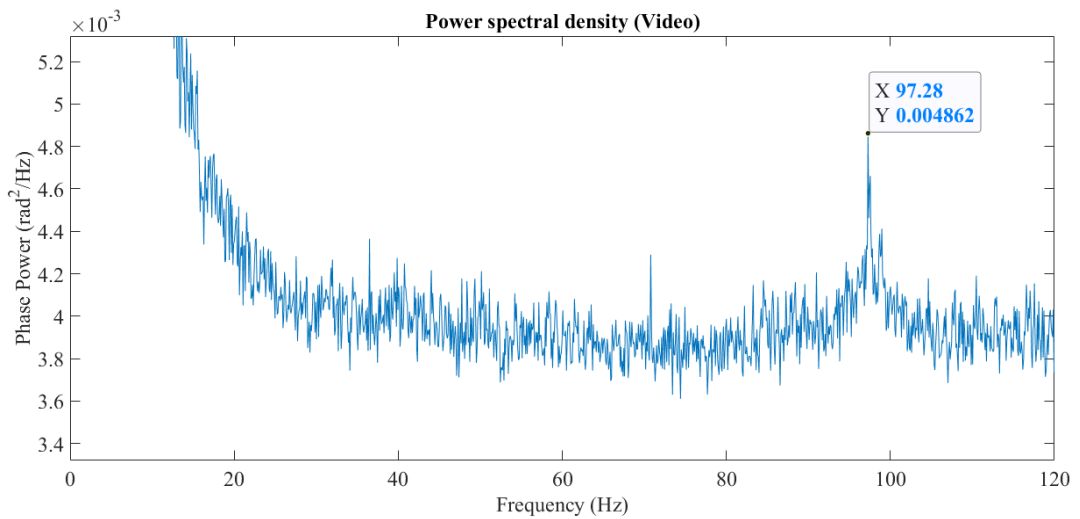


Figure 24. Power spectral density of phase measurement from 2nd left string excited Video-4, with frame rate adjustment to 240 fps

Entry 9, Table 2 shows the relative errors between calibrated values and values extracted from the videos after adjusting frame rate to 240 fps. As it can be seen, errors for 1st left string are 0.00% and 0.31% for two measurements, and for 2nd left string error is 0.71% for both recordings. Error in such a small percentile verifies that the actual frame rate of the camera recordings is 240 fps, even though the details of the videos show various information about the frame rate.

Besides, small error verifies that method is working properly even if the camera was steadied by hand. Therefore, it can be concluded that camera wondering does not affect phase-based motion magnification.

Original frames and magnified frames are illustrated in Figure 25 for first left string and in Figure 26 for second left string. For better visualization of first bending mode of the strings, magnified mode shapes are illustrated with green reference line, where line represents string position at original frame (Figure 25c and 26c).

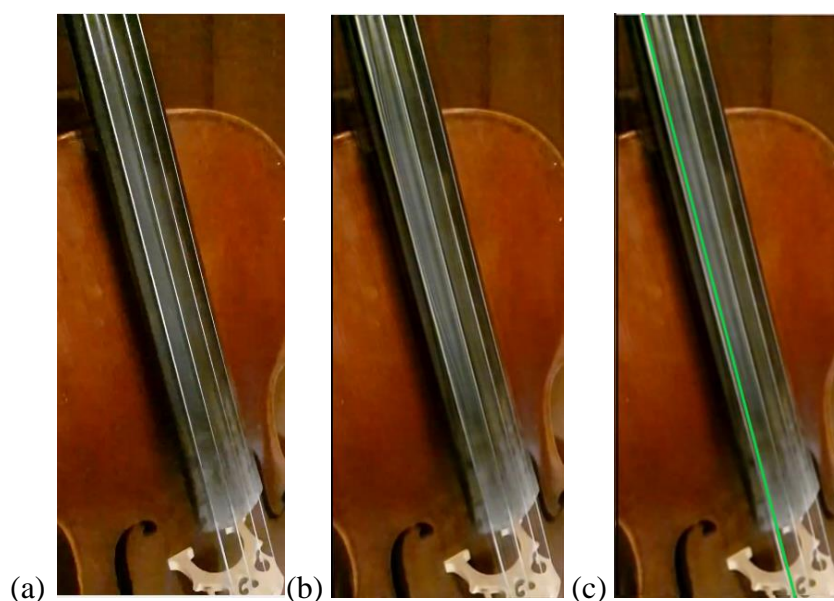


Figure 25. 1st left string motion magnification: (a) Original frame, (b) 20 times magnified frame, (c) magnified frame with reference line.

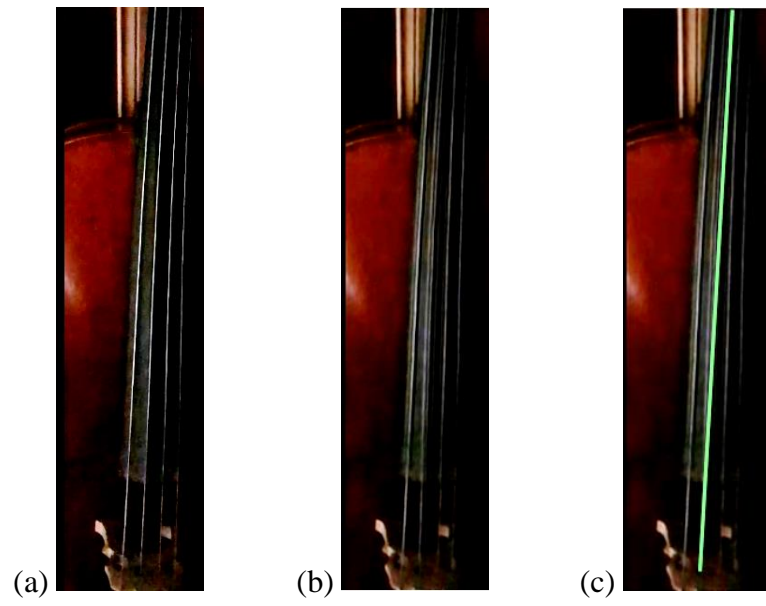


Figure 26. 2nd left string motion magnification: (a) Original frame, (b) 40 times magnified frame, (c) magnified frame with reference line.

CHAPTER 4

MODAL IDENTIFICATION OF METU BRIDGE

4.1. Bridge Architecture

METU A1 Bridge (Figure 27) is actively used pedestrian overpass. It connects shopping malls, DSI, and METU campus and lays over one of the most crowded highways in Ankara, Eskisehir Yolu. So, it is actively used by both university students and DSI workers as well as shopping mall visitors. Besides it experiences a lot of extra vibrations from large number of cars and heavy vehicles passing under it. Therefore, to assure public safety, the proper structural health monitoring of this bridge cannot be neglected.



Figure 27. Side view of METU A1 Bridge (from East to West view)

METU A1 Bridge is a cable stayed bridge which was constructed in 2005. Two abutments of the bridge are made of concrete material, they serve as a support for the deck, which consists of steel beam and concrete cover. Deck is connected to the 43.12 m tall tower with 12 solid steel cables, each with 60 mm diameter. The pylon is anchored to a concrete block from the rear side with additional 12 solid steel cables of same diameter. The bridge has a length of 48.45 m with 3.00 m width. The weight of the pylon is 100 tons, the deck and the cables are 90 tons; in total structure weights approximately 190 tons. The detailed side view drawing of the METU A1 pedestrian bridge is illustrated on Figure 28.

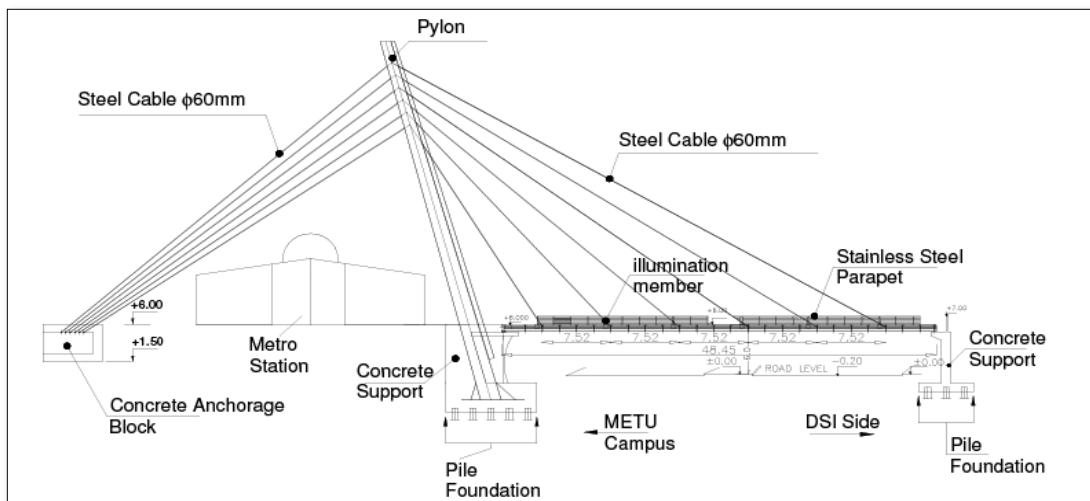


Figure 28. Side view drawing of METU A1 Bridge (Özerkan 2015)

The load of the bridge in longitudinal direction is carried by two pipe sections and three hollow sections that serve as deck support. The former is used in the edges of the bridge and has 300 mm outer diameter and wall thickness of 7 mm. The later made of steel plates with 10 mm thickness and additional 20 mm thick plates are used to stiffen the beam at the junctions with the transverse beams. The longitudinal pipe and box beams are connected by transverse beams. The transverse beams are built-up

I-section that varies in height, being 800 mm in the middle and gradually decreases to 300 mm to the ends, as illustrated in cross section view (Figure 29). The web and flanges of I-section of these beams are in 10 mm thickness, while the width of the flanges is 250 mm. There are 12 transverse beams along the deck between two abutments, located at 1.88 meters apart from each other. The bridge floor constructed with 10 mm thick steel plate slab at the bottom, 5 cm thick mortar with 6 mm in diameter meshed reinforcement at the middle and tiles at the top.

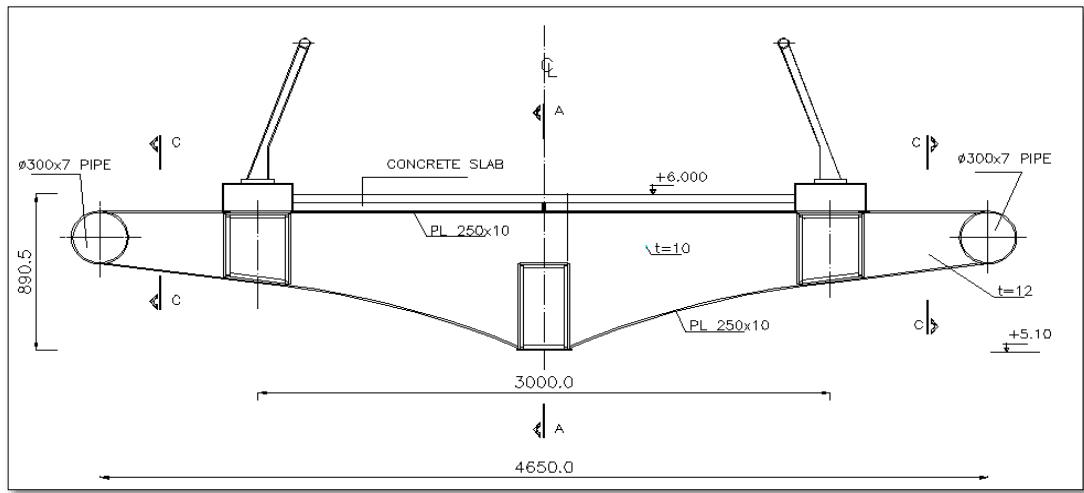


Figure 29. Cross section of METU bridge before addition of billboards (Özerkan 2015)

In couple of years after construction was completed, advertisement billboards were placed on both sides of the bridge. The steel frames of the billboards are connected to the circular pipe section at the end of cross section. Revised cross section of the bridge with addition of advertisement billboards is shown in Figure 30.

These billboards not only provided different physical appearance to the overpass, but also created additional load on a bridge that already suffers large

pedestrian live load. Attaching advertisement billboards, influenced not only weight but also stiffness of the structure of the bridge.

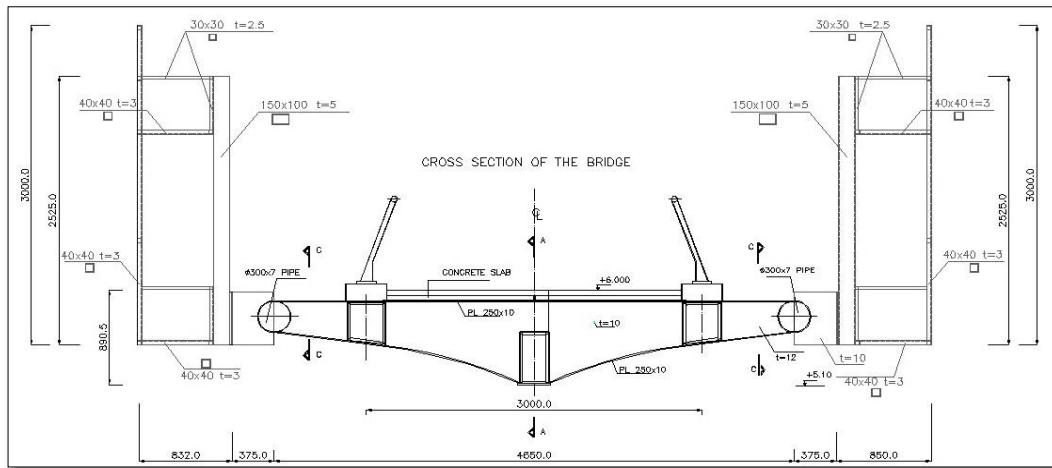


Figure 30. Cross section of the bridge with additional billboards

4.2. Measurements with accelerometer

For the modal identification of the bridge, accelerometer of the smartphone was used. In order to obtain main torsional mode along axial direction and bending mode frequencies of the bridge, accelerometer was placed in different places. The sensor was placed to the middle and 2/3 of the span with varying corners and middle of the width of the bridge deck.

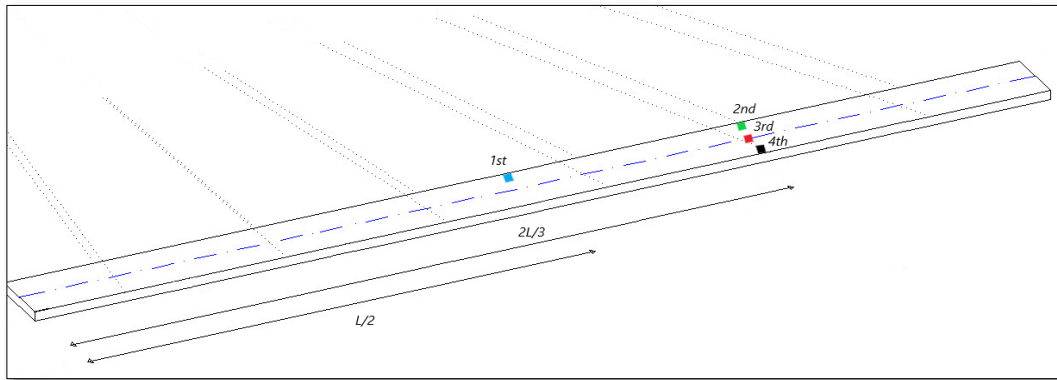


Figure 31. Sketch of placement of accelerometer measurements

First reading was measured at the middle of the span and the at the left edge of the width of the bridge, while the second one at the $2/3$ of the span and the same edge of the width. For the third reading measurements at the $2/3$ the span and the at the middle of the width were taken. As for the last, fourth reading of the accelerometer was located at the $2/3$ of the span and the at the right edge of the width. Places of 4 different measurements are shown in different color in Figure 31.

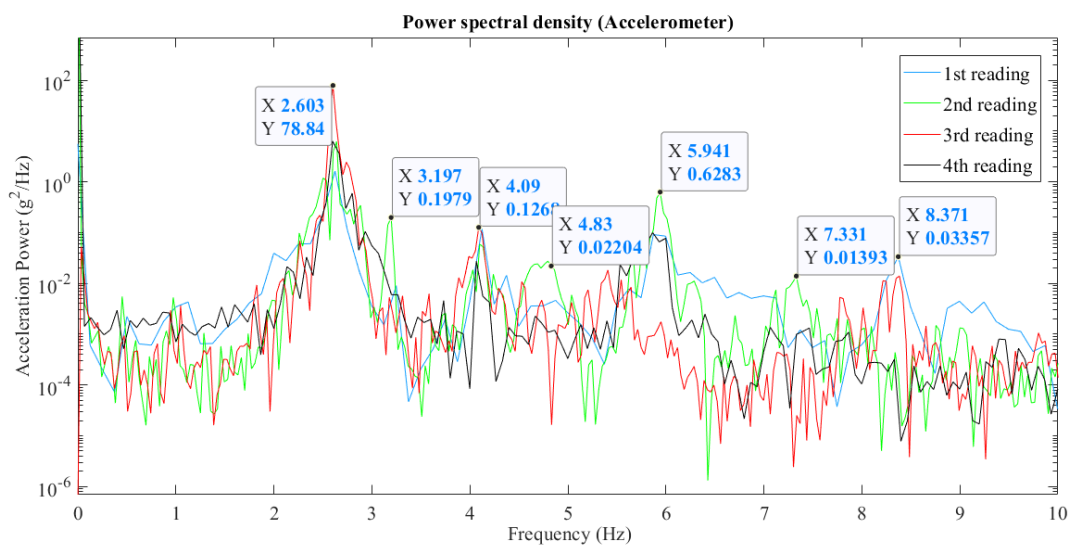


Figure 32. Frequency spectrum of 4 different measurements

Natural vibrational frequencies can be identified by looking at frequency spectrum of accelerometer readings (Figure 32). Figure 32 shows frequency spectrum of vertical acceleration measurements that were taken from four different places on the bridge deck. The readings of the vertical acceleration were continued approximately 30 seconds which gives sampling rate of 0.0338 Hz on frequency spectrum.

In order to find bending and torsional modes vertical vibrational signals are taken to account. To separate bending modes from torsional modes the third reading was taken into account, which represents data taken from accelerometer at the mid width of the bridge. At this location accelerometer should not detect any vibration coming from torsional mode. Therefore, first, second, and fourth bending modes are clearly seen as 2.6 Hz, 4.09 Hz, and 8.37 Hz, respectively. However, third bending mode is not easy to identify because of mismatching of third reading with other readings. Assuming that at third reading accelerometer is placed at nodal point of the related bending mode and taking other readings to account third bending mode frequency is chosen as 5.94 Hz.

Since vertical resonance frequencies show only bending and torsional modes, it is easily possible to assign torsional modes after detecting bending modes. In Figure 32 there are seven main peaks, each referring to resonant frequencies. Four of them were previously assigned for first four bending modes. Therefore, remaining three peaks are first three torsional modes which are 3.20 Hz, 4.83 Hz, and 7.33 Hz, respectively. Table 3 summarizes all modes that are extracted from accelerometer data.

Table 3. Vibration modes of the bridge deck from accelerometer measurements

	1	2	3	4
Bending modes (Hz)	2.60	4.09	5.94	8.37
Torsional modes (Hz)	3.20	4.83	7.33	-

4.3. Finite element model (FEM)

To verify that modes are correctly assigned to the corresponding frequencies additional analysis is required. For that purpose, computer model of the monitoring structure, modelled using SAP2000 Finite element modeling program, was used. The program simulates the physical behavior of the structure by dividing the structure into finite number of parts and assigning the material properties, loads, and boundary conditions. The main challenge of the modeling is constructing the geometry of the structure and calibrating the model with measured data.

The FE model of the bridge is found in the literature (Özerkan 2015). However, it did not consider the billboards placed on two sides along the bridge. In order to obtain more precise results, available FE model was used with addition of advertisement panels. The model consists of four main parts: tower, deck, cables, and billboards as shown in Figure 33.

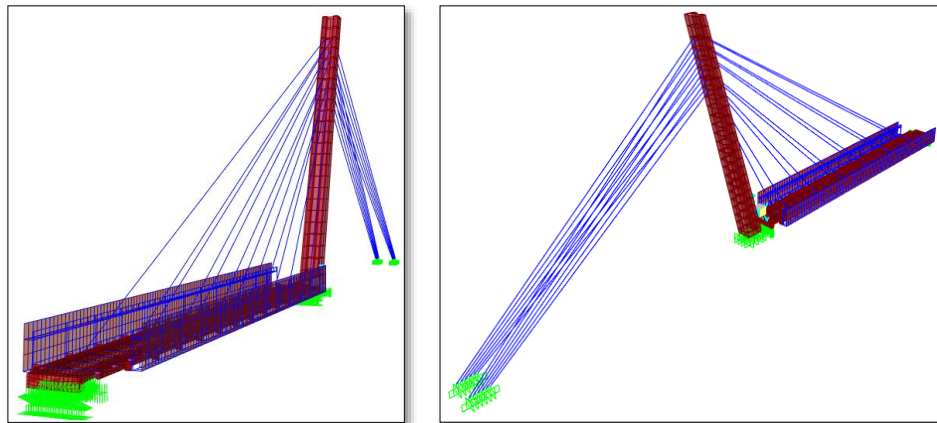


Figure 33. FEM of the bridge

Tower was modeled with 60 mm and 30 mm thick shell members. The sharp corners were strengthened with 10 mm thin triangular shell member to simulate transitions between walls and the base was assumed to be fixed (Figure 34).

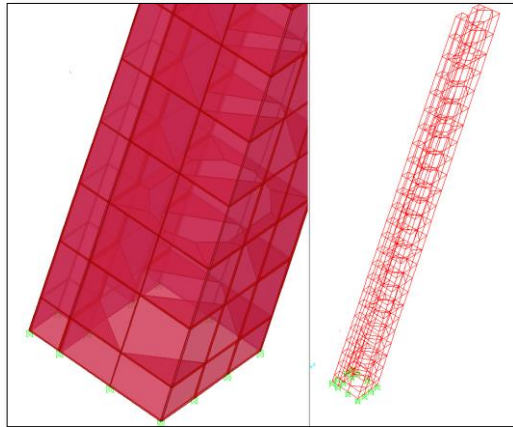


Figure 34. FEM of the tower of the bridge

Deck was constructed with 30 mm, 5 mm, 7 mm, 12 mm, 10 mm thick shell members and 2 frame members, as shown in Figure 35. Shell members are shown in red color, and frame members are illustrated in blue. The frame members were used because shell members were not aligned properly.

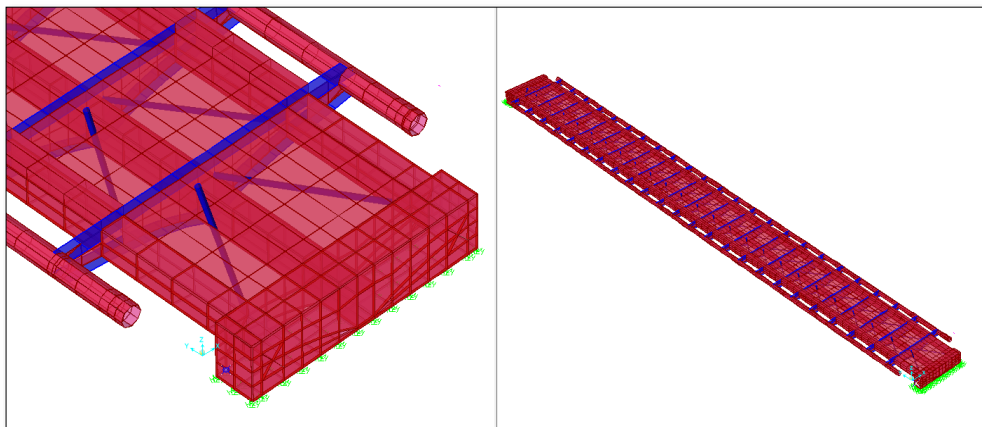


Figure 35. FEM of the deck of the bridge

Cables are constructed as a frame member with 48 mm in diameter. They serve as a truss connection between deck-tower and tower-anchor block. The Figure 36, left, shows how the cables are linked to the deck. While Figure 36, right, demonstrates connections of cables to the tower and the anchor block.

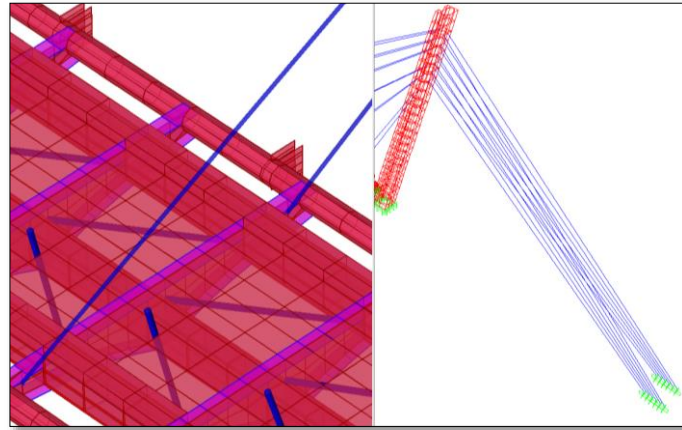


Figure 36. FEM of the cables of the bridge

The FE model from the literature did not include the advertisement billboards that are located on both sides of the deck. However additional weight is present with the presence of that panels. So, the model of the billboards was added, in order to have more accurate model of the bridge.

Billboard was modeled both as a shell model and as frame model in order to compare the results and use better model (Figure 37). While meshing the members the dimension ratio of 1/2 was not exceeded.

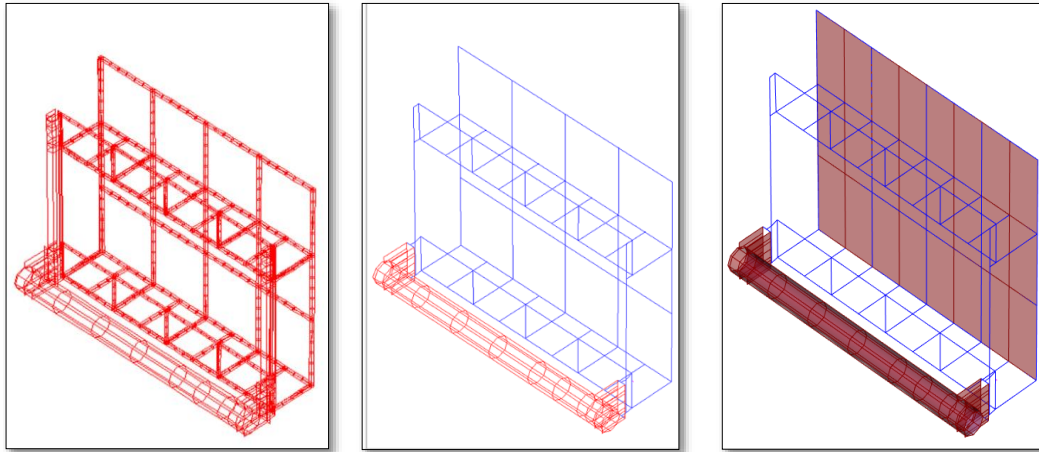


Figure 37. FEM of the billboards on the bridge

After modelling the geometry of the structure, the loads were assigned. Dead load, cover load, couplers load, and prestressing load were considered in the model. The dead load was taken by program itself; the cover load was applied as distributed load 50kN/m^2 , the couplers load was applied as point load 98.07 N and prestressing load was applied as temperature difference to achieve 1 ton for cable between deck-tower, and 3 tons for cable between tower-anchor.

The material properties of members were applied as shown in Table 4.

Table 4. Analysis property data table (Özerkan 2015)

Analysis Property Data	Material
	Steel & Cable mat.
Mass Per Unit Volume	7.85E-09 N/mm ³
Weight Per Unit Volume	7.70E-05 N/mm ³
Modulus of Elasticity	2.10E+05 N/mm ³
Shear Modulus	8.08E+04 N/mm ³
Poisson's Ratio	0.30
Coefficient of Thermal Expansion	1.17E-05

The spring properties of supports of the deck are summarized in Table 5.

Table 5. Table of spring properties of support (Özerkan 2015)

Supports of Deck	Value of stiffness		
	U _x (N/m)	U _y (N/m)	U _z (N/m)
Near Tower	9.81E+07	9.81E+07	9.81E+07
Far from Tower	4412993	4412993	9.81E+07

After constructing the model, the forces and natural frequencies were checked to make sure that they are logically possible.

In order to have accurate data, FE model calibration is needed. Calibration was done in order to match accelerometer values by increasing the weight of the shell members of billboard panels by 1.2 times and 10 mm steel shell member by 2.8 times, which lies under the tile, to compensate the weight of the tile. The stiffness and moment of inertia of shell members and frame members are decreased by 0.7 to

calibrate the FE model. Table 6 summarizes mode frequencies of both calibrated and uncalibrated frequencies of FEM.

Table 6. Mode frequencies of calibrated and uncalibrated models (Hz)

		1	2	3	4
Without Calibration	Bending modes	2.93	5.06	7.80	11.79
	Torsional modes	3.73	7.12	-	-
With Calibration	Bending modes	2.63	4.23	6.61	8.40
	Torsional modes	3.44	4.35	-	-

In Figure 38 (left) the first bending mode shape of FE model is illustrated. The first torsional mode shape of the model is shown in the Figure 38 (right).

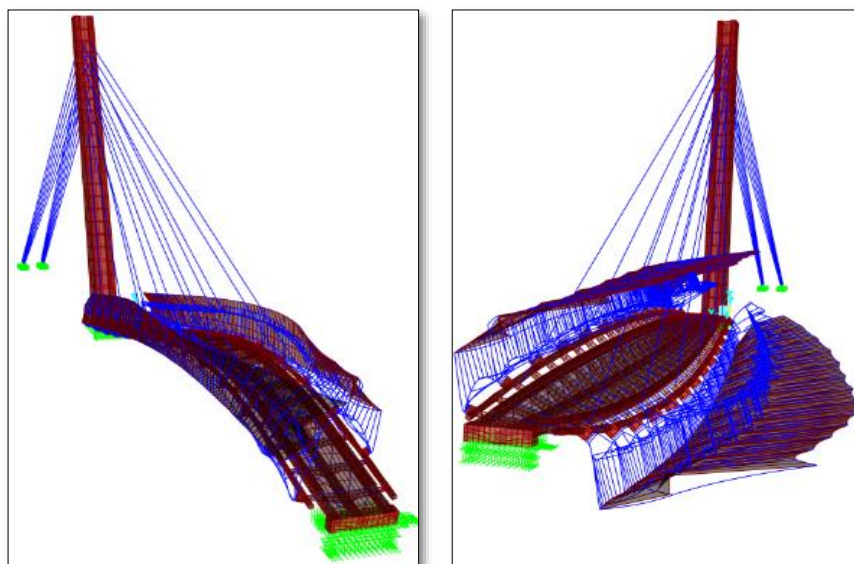


Figure 38. First bending mode 2.63 Hz (left), first torsional mode 3.44 Hz (right)

The second bending mode of the FE model is shown in Figure 39. The left figure reveals the mode shape, where advertisement billboards are hidden for better visualization and the figure in the right shows the same mode shape with exciting billboards. It is true also for the third bending mode (Figure 41), fourth bending mode (Figure 42) and for second torsional mode (Figure 40) of the FE model.

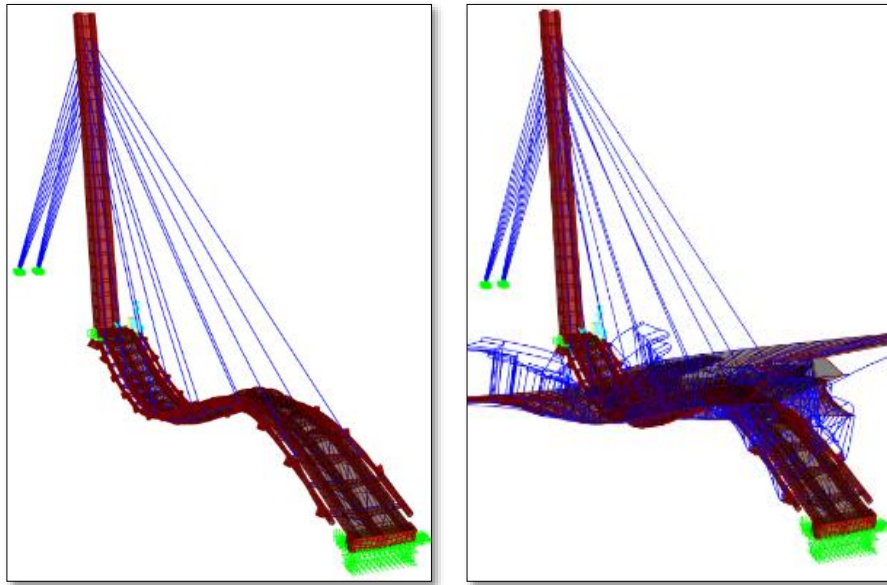


Figure 39. Second bending mode 4.22 Hz: without billboards (left), with billboards (right)

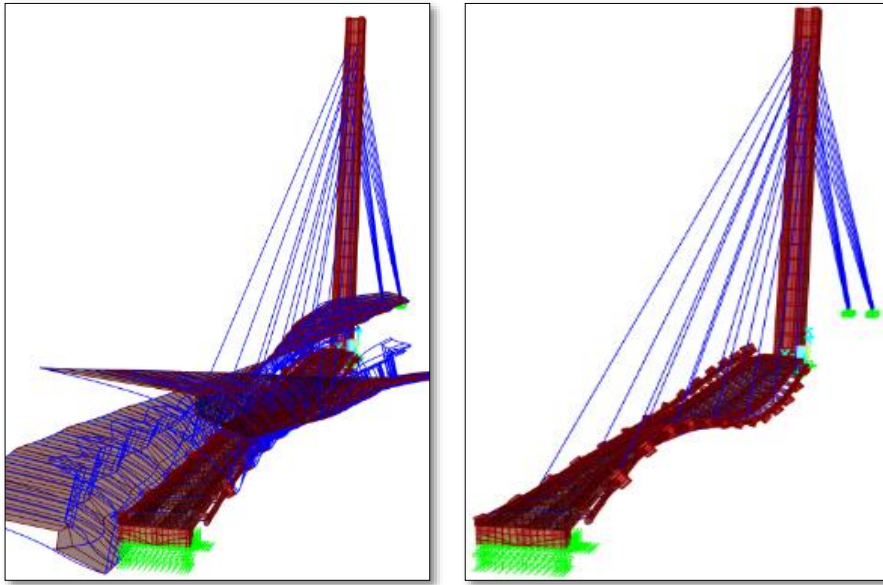


Figure 40. Second torsional mode 4.35 Hz: without billboards (left), with billboards (right)

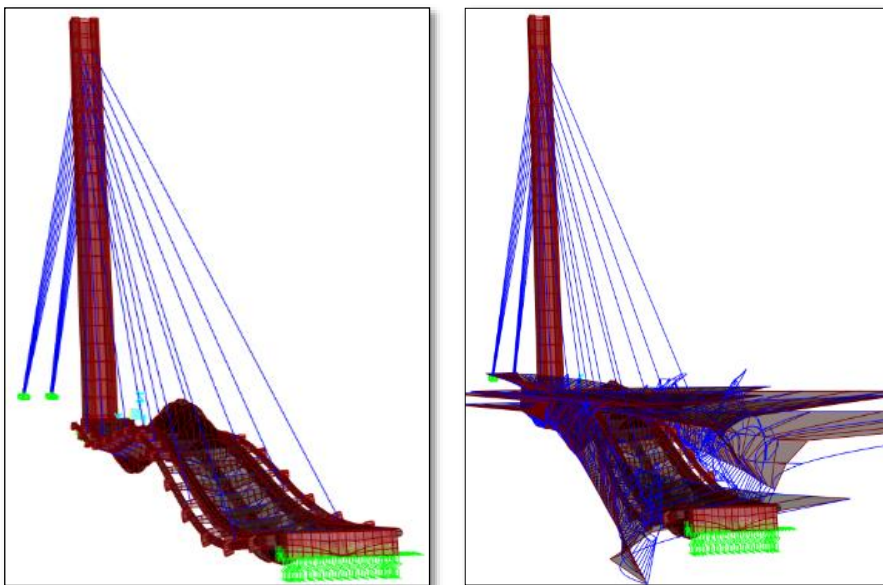


Figure 41. Third bending mode 6.60 Hz: without billboards (left), with billboards (right)

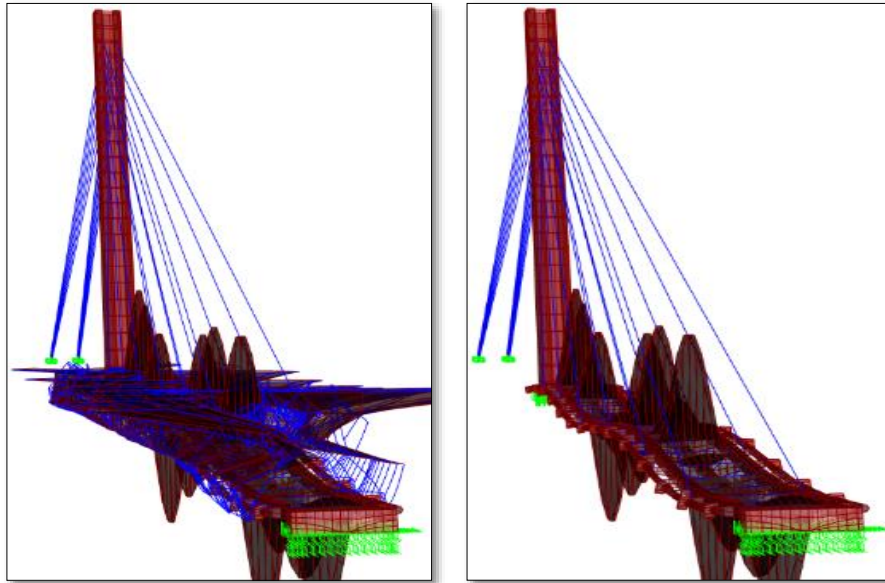


Figure 42. Fourth bending mode 8.40 Hz: without billboards (left), with billboards (right)

4.4. Measurements with camera

4.4.1. Video motion detection

All the camera measurements were done by the simple smartphone, Xiaomi Note 5, having camera adjusted to 60 fps frame rate and 1080x1920 pixels frame dimensions. For frontal view smartphone was placed on tripod at the end of the deck on the opposite side to the tower of the bridge. For the side view, two different captures from both sides, METU side and DSI side, were taken. To guarantee the capture of excited bending and torsional modes, they were stimulated by jumping on the middle of the deck. The outcome video was then processed using phase-based motion magnification algorithm that were verified by ruler and cello experiments mentioned before.

Unfortunately, clear magnified results were not obtained from neither of the side view videos. On the capture from the DSI side, the tree present in the picture does

not allow us to perform proper processing. Meanwhile, the METU side view video process did not give satisfactory amplification results, possibly, due to large distance of capture. Smartphone has better pixel density of the object when it takes video in closer distance to the object, for the captures from large distances, more advance cameras in terms of resolution and optical zoom can be utilized. Since in this thesis only smartphone camera is used, side view motion magnification was not successful. Fortunately, frontal view motion magnification gave acceptable result.

In order to reduce processing time video was shortened to 35 seconds giving 0.0285 Hz sampling rate on frequency spectrum. To avoid magnification of the motion of side billboards and cables, video was cropped focusing only on the deck. Resultant video was processed by using algorithms of phase-based motion detection, explained in theoretical part. Apart from the existing algorithm undercomplete complex steerable filters were used, which detects phase changes in only vertical directions (-11.25° , 0° , $+11.25^\circ$). After processing video with these vertical filters, phase signal for each pixel was obtained. Applying FFT to each pixel and averaging them by amplitude more effective frequency spectrum was obtained which amplifies signals with better edges (amplitudes). In order to obtain whole spectrum of resonant frequencies of bridge deck, 10 points along the left edge of the deck were chosen and their frequency spectra were detected. Average of all 10 spectrums are shown in Figure 43. The reason for selecting only left edge of the deck is that the middle part of the deck does not have very sharp edges and half of the right edge was covered by dynamic load source (jumping man).

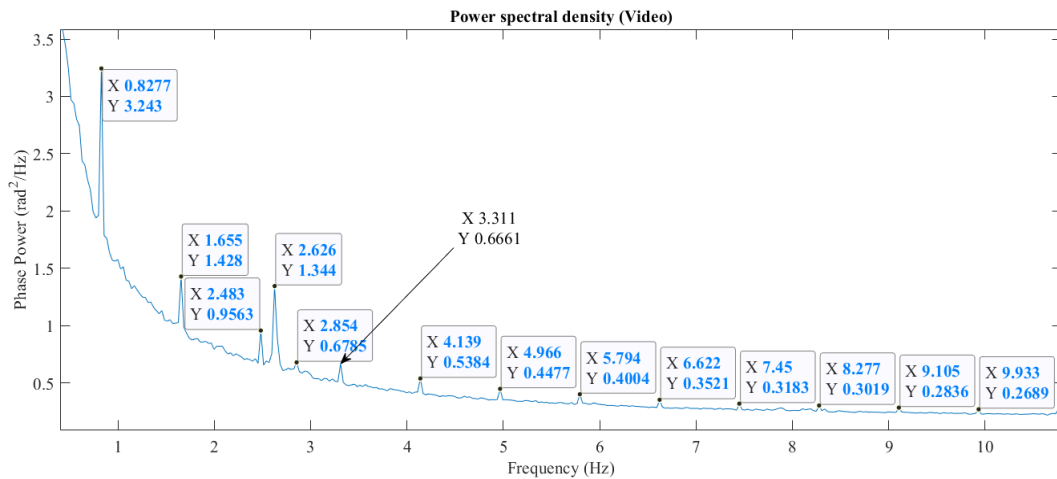


Figure 43. Power spectral density of phase measurements from video

From the Figure 43, it is clearly observed that bridge deck resonates at 2.63 Hz and has one of the most powerful signals with respect to the other mode frequencies which increases the chances to see clear magnification vibration at that frequency. By relying on results of accelerometer measurements and FEM analysis, peaks from frequency spectrum from video processing can be interpreted.

In Figure 43 all of the peaks, except 2.626 Hz and 2.854 Hz, have interval of 0.827 Hz. This pattern of peaks can be behavior of cable resonant frequencies (Lee & Chen, 2004) and definitely not for deck resonant frequencies. When data from the Figure 43, except for 2.626 Hz and 2.854 Hz, are plotted to mode number versus mode frequency graph (Figure 44), the perfect linear relation can be observed. Such perfect fit with regression line of $R^2=1.00$ is unusual for cable behavior. Therefore, the initial assumption that camera was under influence of vibration of the cable was reconsidered as wrong interpretations of the peaks. After obtaining $R^2=1.00$ in Figure 44 and taking into account similar behavior of peaks in ruler experiment in Figure 19, it was concluded that algorithm might produce repeating peaks of first vibrational mode frequency which are not actual peaks but artifacts of first mode.

Therefore, Figure 43 shows only 2 acceptable peaks related to the deck vibration which are 2.626 Hz and 2.854 Hz. Assuming that 2.626 Hz is first bending mode of the deck, the error between video and accelerometer measurements is 1.15%. From low value of error percentile, it was concluded that the phase-based motion detection is applicable for modal identification, at least identification of first bending mode of the 48 m long cable stayed pedestrian bridge. Peak at 2.854 Hz could be considered as first torsional mode since it is the closest point to first torsional mode frequency from accelerometer measurements.

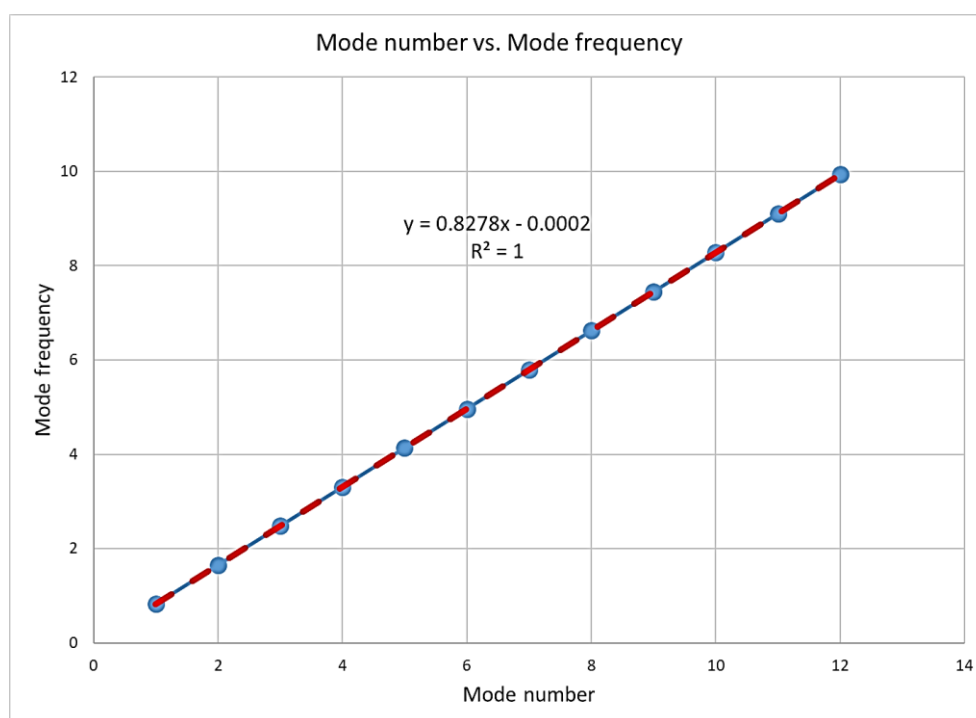


Figure 44. Mode number vs. mode frequency graph of camera motion under influence of cable vibration (all peaks except 2.626 Hz and 2.854 Hz)

4.4.2. Video motion magnification

After detecting the resonance vibration frequencies of the deck with motion detection algorithm, it is possible to verify the findings and interpretations of each

resonant frequencies by magnifying motion and visually identifying the mode shapes of the magnified videos.

Figure 45 demonstrates the frontal view of the bridge, from DSI side. As it can be seen from the left edge of the bridge, on the original frame the edge is straight, shown in green reference line, and no visible bending is present. After processing the video, the large oscillations of first bending mode can be clearly seen. On Figure 45, frame number 255 from the magnified video is illustrated. In this particular frame the middle of the bridge is moved down, shown in red line, without any torsion.

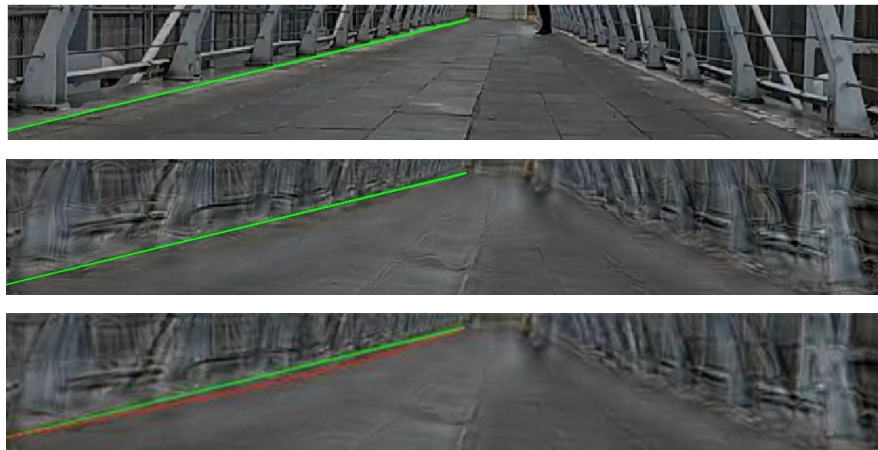


Figure 45. 255th frame original frame and magnified frame (2.6 - 2.7 Hz)

The motion of the middle of the bridge in upside direction corresponds to frame number 267 in magnified video which is shown in Figure 46. Here as well, left edge of the bridge is straight for the original frame, shown in green reference line, and bending is seen only after proper amplification, shown in red line.

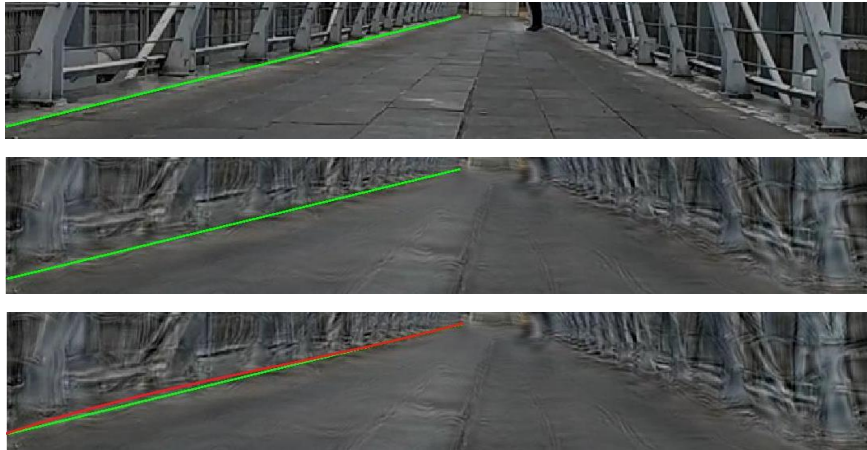


Figure 46. 267th frame with magnified frequency band 2.6 - 2.7 Hz

Difference between maxima and minima frames shows that the magnified motions are in a range of 2.6 -2.7 Hz, which is exactly what is expected for first bending mode, according to the results of accelerometer.

4.5. Discussion and comparison

Using phase-based motion magnification algorithm and simple smartphone video, without any additional surface preparation first bending mode of the bridge deck was successfully obtained. The first bending mode of the deck is not only seen with naked eyes on magnified video but also numerical value agrees with the value obtained using accelerometer. From the frequency spectrum of the video first mode frequency was found to be 2.63 Hz with sampling rate 0.0285 Hz, while accelerometer frequency spectrum indicates that the first mode is 2.60 Hz with sampling rate of 0.0338 Hz. As it can be seen from Table 7, the value from video lies within the range of sampling rate of accelerometer.

Table 7. Comparison table of calibrated FEM, accelerometer measurements and video measurements

	Mode type	1	2	3	4
Calibrated FEM	Bending modes	2.63	4.23	6.61	8.40
	Torsional modes	3.44	4.35	-	-
Phone-based Accelerometer	Bending modes	2.60	4.09	5.94	8.37
	Torsional modes	3.20	4.83	7.33	-
	Sampling Rate	0.0338			
Video	Bending modes	2.63	-	-	-
	Torsional modes	2.85	-	-	-
	Sampling Rate	0.0285			
Error between accelerometer and video values	Bending modes	1.15 %	-	-	-
	Torsional modes	10.9 %	-	-	-

Note: all values are given in Hz.

The FE model was calibrated to match bending mode values found by accelerometer. Using this FE model, the first and second torsional modes found to be 3.44 Hz and 4.35 Hz, respectively. Although it was hard to assign torsional modes using accelerometer measurements, previously with no additional data it was assigned that first two torsional modes are 3.20 Hz and 4.83 Hz. The calibrated FE model approves that these values were assigned correctly.

CHAPTER 5

CONCLUSION

A novel approach to video-based modal analysis has been investigated; previously developed code was improved and successfully tested on a number of structures. Main contribution to the state-of-the-art was addition of a code to search for video-based frequencies that resonant motion exists and then targeting the software towards the identified frequencies to obtain visual amplified mode shapes from the video recording. The existing algorithm (Wadhwa, 2013) was modified and improved in such a way that the frequency band for the magnified motion in output video is found automatically and more accurately. After successful video processing, all obtained data are compared with the data taken from accelerometers and FE model to verify the results.

Obtained structural response decomposition based on video magnification were mostly limited to the first mode shape or two because of the video frame recording speed, video resolution, and computer RAM & computing power limitations. Video-based motion magnification was first tested on simple structures such as a 1m long steel ruler and a cello C2 and G2 strings. Similar to the cello, bridge cable vibrations were obtained with better accuracy and larger number of vibration modes were possible to capture when compared to the METU A1 Bridge case since the cable vibration displacement amplitudes were larger than the METU A1 Bridge case. Nevertheless, it was possible to capture vibration frequency matching with the accelerometer measurements and magnify the first bending mode video of the METU A1 Bridge. The results also compared nicely with the calibrated bridge FEM. Phase-based video magnification method is deemed to be successful based on good match with accelerometer results of ruler, tuning calibrator adjusted cello string frequencies, tested and calibrated FEM of METU A1 Bridge, and visual inspection of METU A4

Bridge cable. Obtained results gave acceptably good agreement for METU A1 Bridge as 2.60 Hz for accelerometer, 2.63 Hz for FE model, and 2.63 Hz for the video motion detection results.

In addition to quantitative vibration frequency results of video motion detection, video motion magnification method provides a real image motion – animation for the mode shapes at determined resonant vibration frequencies. Obtaining video animation for determined frequencies is an important outcome and advantage of this approach. Since every pixel serve as a sensor for small motions, this thesis provides a cost efficient and powerful technique for mode shape and modal frequency identification.

It is concluded that slight camera wondering does not play an important role in phase-based motion magnification for successful amplification of the first vibration mode of cello strings. The analysis is based on a cropped area of video that includes the vibration section of the analyzed structure. If the wondering is too large to move the cropped area away from the vibrating structure, the results would be unsuccessful. Otherwise, low frequency wondering motion does not interfere with the relatively high frequency structural vibration motion. When the cello example was considered, resonant vibration frequency of the strings at about 65 Hz and 98 Hz; while, the hand vibrations were in much lower frequency, i.e. less than 10 Hz. Cello string was recorded at 240 Hz and frequencies up to 120 Hz were possible to be captured.

An additional observation about the video recording was erroneous sampling frequency information in the recorded video files. Although video sampling was 240 fps, some of the video files indicated various frequencies changing from 180 fps to 210 fps. If the recorded file “frame per second” (fps) information was directly used, wrong resonant vibration frequencies were obtained.

Video-based frequency space decomposition generated some artefacts of the first resonant mode that repeats itself with constant intervals. The regression fit R^2 of 1.00 was obtained using the consecutive peak frequencies which is unusual to obtain

in nature. Bridge example thought to be the contribution of consecutive cable vibration frequencies; however, same effect was observed in the ruler example and was identified as a procedure problem. Cello string was not able to reproduce similar effect since the resonant vibration was too close to the Nyquist frequency.

5.1. Limitations of current study

The main reason why higher resonant modes of the bridge deck were not observed using phase-based motion magnification is due to the fact that high-resolution video camera recording was not available. Instead, simple smartphone camera with a Full-HD 1920x1080 pixels resolution was used. Based on experimental results, it can be concluded that resolution of utilized smartphone was not enough to detect the motion of higher modes. Higher modes have smaller deflections and requires faster frame per second recording speed. Using a camera with higher pixel resolution and faster frame per second recording speeds, it is expected to capture higher modes more efficiently. Optical zoom to a single moving point may improve the deflection resolution since larger number of pixels would capture much smaller motions; however, this was not recommended since it would not be possible to capture the overall mode shape of a structure by zooming in to a small area like a bolt.

Another reason why higher resonant modes were not observed using current method can be the large demand for processing power of computers. It took about half an hour to process cropped 300x700 pixel video of 6 seconds using a notebook PC with 8 Gb RAM and Intel i5 core processor. The resolution of the video was deliberately reduced to HD format of 720x1280, otherwise RAM was not enough to process video data. Bridge video from a distance gave no results while capturing video by placing camera on the deck over the support yielded better results. However, processing all image instead of a cropped area overloads the computer. In order to overcome this problem, downsizing of original videos was necessary. The loss in resolution has negatively affected motion detection. Using computers with larger

RAM with faster CPU and processing larger view with higher resolution cameras are expected to lead to better results.

Another limitation of the performed experiment on METU A1 Bridge is blocking objects in the video. It is very crucial to capture entire bridge in the video in order to clearly see vibration mode shapes of a bridge. However, in this case clear side view capture was not possible due to various obstacles such as tree blocking some part of the bridge and inability of capturing the video from the middle of the highway. Pedestrian motion on the bridge during recording has very adverse effects on the video processing and yields no results. The video should be taken without visual obstacles or moving objects on the structure.

Although first bending mode shape was observed on deck view video, higher modes were not successfully detected since pixels are not evenly distributed (farther parts of the bridge had less pixel density on the recorded video). In other words, the near end of the bridge deck is seen bigger and occupies larger number of pixels, while farther end is seen less and smaller number of pixels contain data of that end. Therefore, the view angle and pixel intensity have effects on the results.

A final limitation is stemmed from the placement of camera on the bridge deck itself or ambient vibration on the camera. If the camera is placed on the bridge deck, it would also vibrate as a function of the bridge response. The background of the bridge then would vibrate based on the camera motion, which is not realistic. A code was prepared for image stabilization if large motion exists such as holding by hand or placing on the bridge deck; however, the image stabilization algorithm had minor success for small vibrations. It is recommended that the camera would be placed on supports that would hold it still, isolate it from the ground, and have no motion at all including interaction with the bridge vibrations. Such an isolation from the environment might be problematic in windy conditions, since wind would cause motion of the camera if isolated from the ground. A heavy base for the camera and suspension from the environment might be advantageous.

5.2. Future work

As for the future work, it is thought to try application of different filters to see if any improvements are possible to achieve using currently developed method.

The developed method can be transferred to mobile platform with proper mobile developer and advanced technologies to make it possible to perform modal analysis of structures only using camera and processing power of a smartphone; since, smartphones are replacing computers in many different aspects of life.

REFERENCES

- ASCE. (2017). *Water Infrastructure | ASCE's 2017 Infrastructure Report Card*. American Society of Civil Engineers.
- Avitabile, P. (1999) Back to basics. *Exp Tech* 23, 17–18.
<https://doi.org/10.1111/j.1747-1567.1999.tb01563.x>
- Baqersad, J., Poozesh, P., Niezrecki, C., & Avitabile, P. (2017). Photogrammetry and optical methods in structural dynamics – A review. *Mechanical Systems and Signal Processing*. <https://doi.org/10.1016/j.ymsp.2016.02.011>
- Caetano, E., Silva, S., & Bateira, J. (2011). A vision system for vibration monitoring of civil engineering structures. *Experimental Techniques*. <https://doi.org/10.1111/j.1747-1567.2010.00653.x>
- Chen, J. G., Wadhwa, N., Cha, Y. J., Durand, F., Freeman, W. T., & Buyukozturk, O. (2015). Modal identification of simple structures with high-speed video using motion magnification. *Journal of Sound and Vibration*, 345, 58–71.
<https://doi.org/10.1016/j.jsv.2015.01.024>
- Farrar, C. R., & Jauregui, D. A. (1998). Comparative study of damage identification algorithms applied to a bridge: II. Numerical study. *Smart Materials and Structures*. <https://doi.org/10.1088/0964-1726/7/5/014>
- Keuwlsoft. (2015). Accelerometer Meter (version 1.32) [Mobile app]. App Store.
<https://play.google.com/store/apps/details?id=com.keuwl.accelerometer&hl=tr>
- Lee, Z. K., & Chen, C. C. (2004). Cable Force Analysis of Gi-Lu Cable-Stayed Bridge after Gi-Gi Earthquake. *Iabmas04*.
- Nassif, H. H., Gindy, M., & Davis, J. (2005). Comparison of laser Doppler vibrometer with contact sensors for monitoring bridge deflection and vibration. In *NDT and E International*. <https://doi.org/10.1016/j.ndteint.2004.06.012>

- Özerkan, T. (2015) Instrumented monitoring and dynamic testing of METU cable stayed pedestrian bridge and comparisons against the analytical model simulations, M.S. Thesis, Middle East Technical University
- Rubinstein, M. (2014). Analysis and visualization of temporal variations in video. Retrieved from <http://dspace.mit.edu/handle/1721.1/87934%0Apapers2://publication/uuid/2298C880-2177-4B5B-B9CE-2378E3368B01>
- Sarrafi, A., Mao, Z., Niezrecki, C., & Poozesh, P. (2018). Vibration-based damage detection in wind turbine blades using Phase-based Motion Estimation and motion magnification. *Journal of Sound and Vibration*, 421, 300–318. <https://doi.org/10.1016/j.jsv.2018.01.050>
- Shang, Z., & Shen, Z. (2017). Multi-point Vibration Measurement for Mode Identification of Bridge Structures using Video-based Motion Magnification Keywords. Retrieved from <http://arxiv.org/abs/1712.06566>
- Skurowski, P., & Gruca, A. (2009). Image quality assessment using phase spectrum correlation. In *Lecture Notes in Computer Science (including subseries Lecture Notes in Artificial Intelligence and Lecture Notes in Bioinformatics)*. https://doi.org/10.1007/978-3-642-02345-3_9
- Wadhwa, N. (2016). Revealing and analyzing imperceptible deviations in images and videos.
- Wadhwa, N (2013) Phase-based motion magnification source code (Version 1.0) [Source code]. <http://people.csail.mit.edu/nwadhwa/phase-video/>
- Yang, Y., Dorn, C., Mancini, T., Talken, Z., Nagarajaiah, S., Kenyon, G., ... Mascareñas, D. (2017). Blind identification of full-field vibration modes of output-only structures from uniformly-sampled, possibly temporally-aliased (sub-Nyquist), video measurements. *Journal of Sound and Vibration*, 390, 232–256. <https://doi.org/10.1016/j.jsv.2016.11.034>

APPENDICES

A. Additional accelerometer measurements on METU A1 Bridge deck

Additional measurement with G-Link-LXRS MicroStrain triaxial MEMs accelerometers was performed. Measurement rate was set to 256 Hz and readings were continued to 40 seconds. All readings were started simultaneously at the same time. The sketch of the placement of the accelerometers is shown in Figure 47.

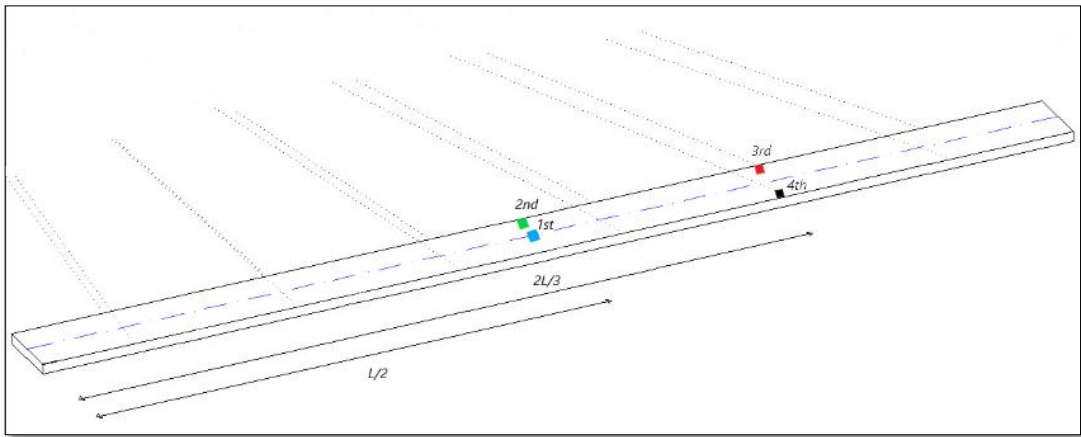


Figure 47. Sketch of placement of accelerometer measurements

Figure 48 shows frequency spectrum of the measurements, where 4 main peaks represent first four bending modes.

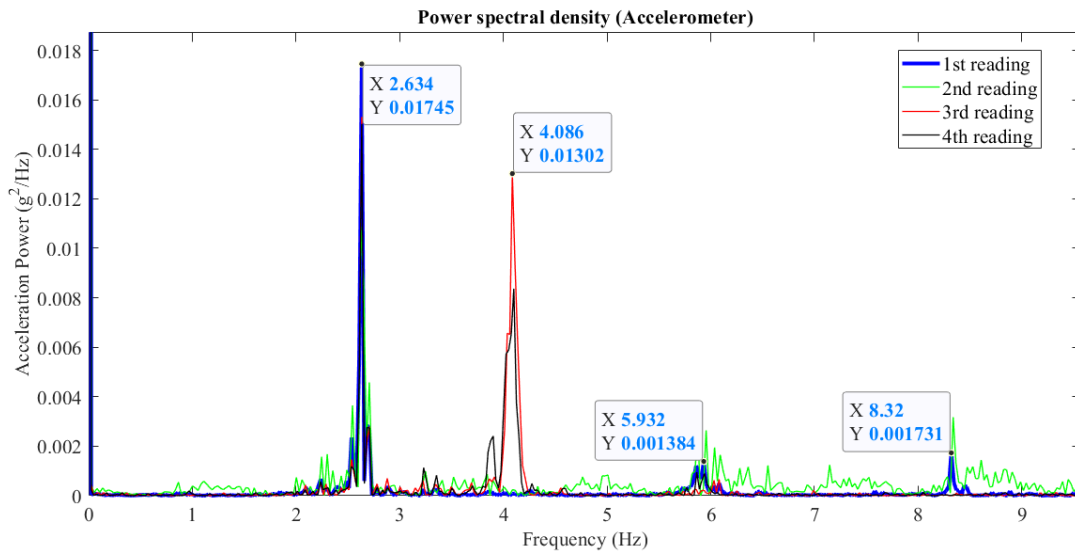


Figure 48. Power spectral density of accelerometer measurements

Peak at 4.09 Hz could be confused with torsional mode, however looking to the imaginary part of Fourier transform of the 3rd and 4th readings shows that this peak represents one of the bending modes. The fact that the imaginary parts of these two readings match each other perfectly in terms of sign of the peaks (Figure 49), proves that peak at 4.09 Hz is one of the bending modes, indeed it is second bending mode. Therefore, it cannot be interpreted as torsional mode.

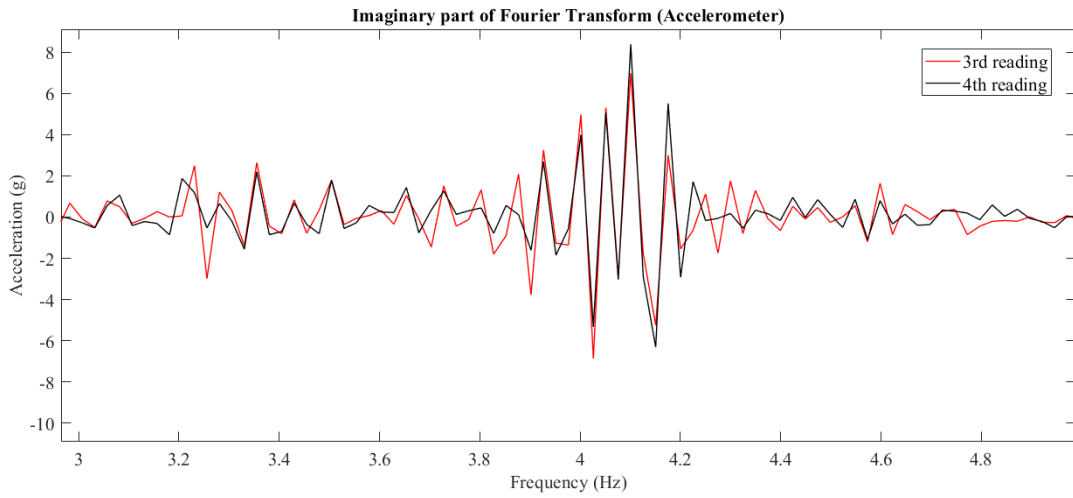


Figure 49. Imaginary parts of Fourier transforms of 3rd and 4th readings

For torsional mode the peaks for two readings must have different sign of the amplitude of the peak, if one has plus sign the other reading must have negative sign at the same frequency (Avitabile, 1999).

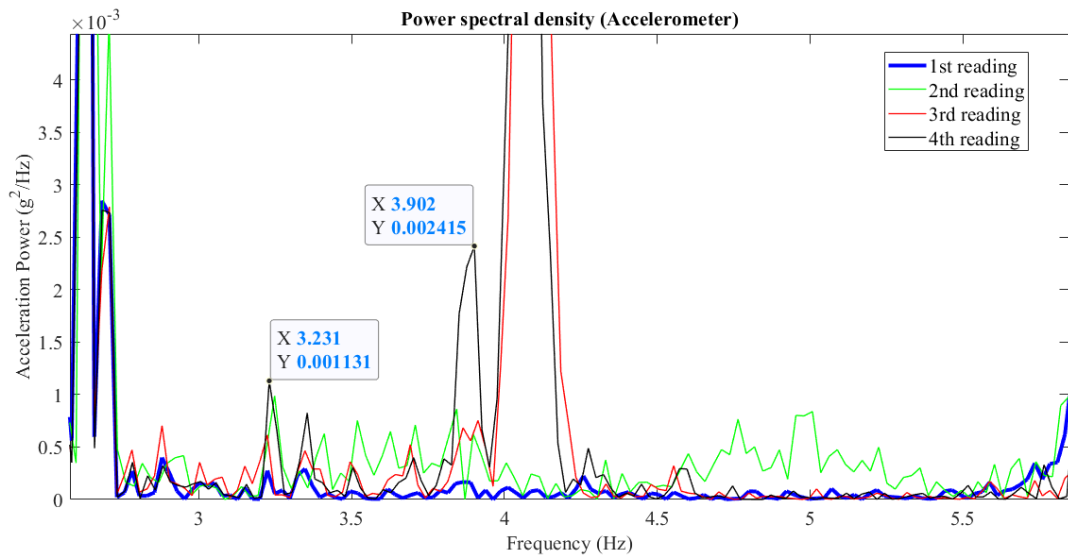


Figure 50. Zoomed power spectral density of accelerometer measurements

Figure 50 shows that there are two peaks, 3.23 Hz and 3.90 Hz, that were seen in all readings except for 1st reading which settled in the middle and cannot catch torsional mode. Therefore, these peaks could be falsely assigned to be torsional modes. The additional information from the plot of the imaginary parts of 3rd and 4th readings (Figure 49) clearly show that there are no any signals belonging to torsional mode in the region between 3 Hz and 4.8 Hz.

The summary of the accelerometer measurements is shown in Table 8.

Table 8. Summary table of resonant frequency modes of METU A1 Bridge deck from accelerometer measurements

	1	2	3	4
Bending modes (Hz)	2.63	4.09	5.93	8.32
Torsional modes (Hz)	-	-	-	-